P148367.PDF [Page: 3 of 80]

94-613

COMMUNICATIONS
RESEARCH
LABORATORY

SEA SWELL MODELLING, COLLECTION AND ANALYSIS OF DATA

by

P. Bauman
J. Litva
L. Lai
T. Lo

Submitted to
Defence Research Establishment Ottawa
Scientific Authority: E. Bosse

Under DSS Contract W7714-7-5320

Faculty of Engineering
McMaster University
Hamilton, Ontario
Canada L8S 4K1

March 1989

©Her Majesty The Queen in Right of Canada 1989

P148367.PDF [Page: 5 of 80]

105-02513/

CRL REPORT SERIES
CRL–199

SEA SWELL MODELING, COLLECTION AND ANALYSIS OF DATA

P. Bauman, J. Litva, L. Lai, T. Lo
Communications Research Laboratory
McMaster University
Hamilton, Ontario

This report applies to
DSS Contract W7714–7–5320

Communications Research Laboratory
McMaster University
Hamilton, Ontario, Canada
March 1989

CONTENTS

1. INTRODUCTION 3
2. THEORY BEHIND THE SEA SWELL MODEL 3
   2.1 Defining the Sea Surface 4
   2.2 Defining the Scattering Geometry 5
   2.3 Defining the Illuminated Region 6
   2.4 Voltage Summation 9
      2.4.1 Shadowing 10
      2.4.2 Complex Reflection Coefficient 11
      2.4.3 Divergence 12
   2.5 First Order Antenna Theory 13
      2.5.1 Coordinate Rotation 15
      2.5.2 Received Voltage 17
3. DESCRIPTION OF SIMULATION SOFTWARE 19
4. SIMULATION RESULTS 19
   4.1 Interference Pattern Null Spacing 20
   4.2 Interference Pattern Null Location 21
   4.3 Effect of Varying Grid Resolution 21
   4.4 Rough Sea 22
5. CORRELATION HEIGHT ANALYSIS OF EXPERIMENTAL RESULTS 23
   5.1 Introduction 23
   5.2 Lake Huron Data Measurement 23
      5.2.1 Multi–Parameter Adaptive Radar System (MARS) 24
   5.3 Calibration Procedures 27
      5.3.1 IQ Calibration 27
      5.3.2 Far–Field Calibration 29
   5.4 Experimental Results 30
      5.4.1 Alias Tracks 30
      5.4.2 CHA Results 32
6. CONCLUSIONS AND FUTURE WORK 33
7. REFERENCES 34
8. FIGURES 35

1 INTRODUCTION

Previous work has developed the theoretical and practical issues involved in simulating multipath from sea swell surfaces [1,2]. These results are extended in this report, and refinements leading to a currently functional sea swell model are detailed. Consistent behavior is observed regarding null location and spacing, and the interference pattern is seen to be a function of sea state as well as grid resolution. The report also features analysis of experimental data obtained from the Lake Huron trials of Fall 1987. This data, as well as that obtained at the Lake Ontario site during Fall 1988 trials, may be used in future validation of the described sea swell model.

As previously discussed [2], multipath due to ocean surfaces may degrade the accuracy of estimation algorithms as changes in the sea surface lead to fluctuations in the multipath signal, thus introducing measurement instability. The particular estimation algorithm of interest, Correlation Height Analysis (CHA), intrinsically depends on the indirect signal's amplitude, phase, and angle–of–arrival in order to extend the antenna's effective aperture. Thus, "sea swells, being a systematic and regular perturbation to the sea surface, could conceivably introduce biases into CHA tracking results" [1]. The ultimate aim of the study underway is to derive a correction factor that may be applied to CHA angle–of–arrival estimates in order to account for the effects of ocean multipath. The model outlined in this report allows for the computation of multipath scattering from arbitrary sea surfaces based on a defined grid, and is geared specifically to sampled aperture computation.

2 THEORY BEHIND THE SEA SWELL MODEL

Theoretical developments toward implementation of the sea swell model are summarized in the following sections, based on previous work [1,2]. Refinement to the scattered voltage computation is the main enhancement and is discussed in detail, while, for the most part, results from previous work are simply restated for reference purposes. Steps involved in defining the ocean surface, the illuminated region, and the scattering geometry are discussed first, followed by computation of the signal scattered from individual facets and subsequent addition of these multipath contributions at the receiver.

2.1 DEFINING THE SEA SURFACE

A sinusoidal wave surface $z(\underline{r},t)$ is described by:

$$z(\underline{r},t) = A\cos(\omega t - \underline{k}\cdot\underline{r}) = A\cos(\omega t - k_x x - k_y y) \quad (1)$$

where

$\underline{r} = (x, y)$ = point on the wave surface

$\omega = \frac{2\pi}{T}$ = frequency

$k = \frac{2\pi}{L}$ ($k_x = k\cos\theta$, $k_y = k\sin\theta$) = wave number

A = peak–to–peak wave amplitude

L = wavelength

T = wave period

and

θ = propagation angle of the ocean wave with respect to the x–axis, i.e., along the direct transmission path.

Arbitrarily rough surfaces can be described by the superposition of numerous waves with various amplitudes, wavelengths, phases, and propagation angles. To this end, the following summation computes the facet height z_{mn} at grid coordinates (x_m,y_n) and for time t as the superposition of P waves:

$$z_{mn}(x_m,y_n,t) = \sum_{j=1}^{P} A_j \cos\left[\frac{2\pi}{T_j}t - \frac{2\pi}{L_j}[\cos(\theta_j)x_m - \sin(\theta_j)y_n] + \phi_j\right] \quad (2)$$

where ϕ_j, a phase factor for the j'th wave, is introduced for increased generality.

Facet slopes, α_{mn} and β_{mn}, pictured in Figure 1, are obtained by differentiating (2) with respect to x and y:

$$\beta_{mn} = \tan^{-1}\left[\frac{\partial z_{mn}}{\partial x}\right] \quad (3)$$

$$= \tan^{-1}\left[2\pi\sum_{j=1}^{P}\frac{A_j}{L_j}\cos(\theta_j)\sin\left[\frac{2\pi}{T_j}t - \frac{2\pi}{L_j}[\cos(\theta_j)x_m - \sin(\theta_j)y_n] + \phi_j\right]\right]$$

$$\alpha_{mn} = \tan^{-1}\left[\frac{\partial z_{mn}}{\partial y}\right] \tag{4}$$

$$= \tan^{-1}\left[2\pi \sum_{j=1}^{P} \frac{A_j}{L_j} \sin(\theta_j) \sin\left[\frac{2\pi}{T_j} t - \frac{2\pi}{L_j}[\cos(\theta_j)x_m - \sin(\theta_j)y_n] + \phi_j\right]\right]$$

2.2 DEFINING THE SCATTERING GEOMETRY

As illustrated in Figure 2, for the mn'th facet with coordinates x_m and y_n, and height z_{mn}, the facet distances r_1 (to receiver) and r_2 (from transmitter) are

$$r_1 = \sqrt{x_m^2 + y_n^2 + (h_1 - z_{mn})^2} \tag{5}$$

$$r_2 = \sqrt{(r - x_m)^2 + y_n^2 + (h_2 - z_{mn})^2} \tag{6}$$

for flat earth geometry, where r is the transmitter–receiver separation. The facet elevation and azimuthal angles (α and β, respectively) with respect to source (subscript 2) and receiver (subscript 1) are

$$\alpha_1 = \tan^{-1}\left[\frac{h_1 - z_{mn}}{\sqrt{x_m^2 + y_n^2}}\right] \tag{7}$$

$$\alpha_2 = \tan^{-1}\left[\frac{h_2 - z_{mn}}{\sqrt{(r - x_m)^2 + y_n^2}}\right] \tag{8}$$

$$\beta_1 = \tan^{-1}\left[\frac{y_n}{x_m}\right] \tag{9}$$

$$\beta_2 = \tan^{-1}\left[\frac{y_n}{(r - x_m)}\right] . \tag{10}$$

Corrections are required for the curved earth geometry shown in Figure 3, modifying (5–8) as follows:

$$r_1 = \sqrt{x_m^2 + y_n^2 + (h_1 - z_{mn} + \Delta(h_1 x))^2} \tag{5'}$$

$$r_2 = \sqrt{(r - x_m)^2 + y_n^2 + (h_2 - z_{mn} - \Delta(x h_2))^2} \tag{6'}$$

$$\alpha_1 = \tan^{-1}\left[\frac{h_1 - z_{mn} + \Delta(h_1 x)}{\sqrt{x_m^2 + y_n^2}}\right] \tag{7'}$$

$$\alpha_2 = \tan^{-1}\left[\frac{h_2 - z_{mn} - \Delta(x h_2)}{\sqrt{(r - x_m)^2 + y_n^2}}\right] \tag{8'}$$

where the curved earth correction factors are given by

$$\Delta(h_1 x) = \frac{x_m^2}{2 \cdot a_e} \tag{11}$$

and

$$\Delta(x h_2) = \frac{(r - x_m)^2}{2 \cdot a_e} \quad . \tag{12}$$

It is assumed that earth curvature is insignificant in the y direction, hence β_1 and β_2 remain unmodified, since it shall be seen that the region of interest is narrow in width relative to length.

2.3 DEFINING THE ILLUMINATED REGION

Fresnel zones are ellipsoidal regions of constant path length and thus phase difference [3] where the locus of the ellipse corresponds to the specular reflection point (see Figure 4) .The centre (x_{on}) and intercept of the semimajor (x_{in}) and semiminor (y_{in}) axes of the n'th ellipse are given by:

$$x_{on} \simeq \frac{r}{2} \frac{1 + \frac{2h_2(h_1 + h_2)}{n \lambda r}}{1 + \frac{(h_1 + h_2)^2}{n \lambda r}} \tag{13}$$

$$x_{in} \simeq \frac{r}{2} \frac{\sqrt{1 + \frac{2\,\delta_0}{n\,\lambda}}}{1 + \frac{(h_1 + h_2)^2}{n\,\lambda\,r}} \tag{14}$$

$$y_{in} \simeq \frac{\sqrt{n\,\lambda\,r}}{2} \sqrt{\frac{1 + \frac{2\,\delta_0}{n\,\lambda}}{1 + \frac{(h_1 + h_2)^2}{n\,\lambda\,r}}} \tag{15}$$

where

$$\delta_0 = \frac{2\,h_1\,h_2}{r} \tag{16}$$

and

r = distance between the source and field points (range),
h_1 = height of the field point (receiver height)
h_2 = height of the source (transmitter height),
λ = signal wavelength .

The illuminated region is taken as the area defined by the sixth Fresnel zone [1] and to simplify the formulation, the length and width of this zone are used to define a rectangular, rather than ellipsoidal area. Origin and intercept values are used to compute the front and back coordinates (x_f and x_b, respectively), as well as left and right coordinates (y_l and y_r, respectively) of the illuminated region:

$$x_f = \frac{r}{2} \frac{1 + \frac{2h_2(h_1 + h_2)}{6\,\lambda\,r} + \sqrt{1 + \frac{2\,\delta_0}{6\,\lambda}}}{1 + \frac{(h_1 + h_2)^2}{6\,\lambda\,r}} \tag{17}$$

$$x_b = \frac{r}{2} \frac{1 + \frac{2h_2(h_1 + h_2)}{6\,\lambda\,r} - \sqrt{1 + \frac{2\,\delta_0}{6\,\lambda}}}{1 + \frac{(h_1 + h_2)^2}{6\,\lambda\,r}} \tag{18}$$

$$y_r = \frac{\sqrt{6\lambda r}}{2} \sqrt{\frac{1 + \frac{2\delta_0}{6\lambda}}{1 + \frac{(h_1 + h_2)^2}{6\lambda r}}} \tag{19}$$

$$y_l = -y_r \tag{20}$$

Note that all variables with subscript "1" refer to antenna while subscript "2" denotes source (for example, h_2 = source height). The origin is assumed to be located at the receiver.

After defining the illuminated region, this area is divided into a grid (i.e., the reflecting facets) at a user–defined resolution in both x and y. Given M grid points in the x direction and N grid points in the y direction, the facet area A is given by:

$$A = \frac{(x_f - x_b)}{M} \cdot \frac{(y_r - y_l)}{N} \quad . \tag{21}$$

The coordinates of the grid centres (x_m, y_n) are given by:

$$x_m = \sum_{i=0}^{M-1} x_f - \frac{(2i - 1)}{2} \cdot \frac{(x_f - x_b)}{M} \tag{22}$$

$$y_n = \sum_{i=0}^{N-1} y_l + (2i - 1) \frac{y_r}{N} \quad . \tag{23}$$

A weighting factor after White and Gery [4] may be applied to the signal voltages scattered from the facets across the first six Fresnel zones to help reduce spurious end effects. These effects are manifested during Cornu spiral construction when adding facet multipath contributions along a strip in range (i.e., y_n held constant). The weighting function w_{mn} is extended to both x and y dimensions and is defined as:

$$w_{mn} = \left\{3t_n^2 - 2t_n^3\right\} \cdot \left\{3t_m^2 - 2t_m^3\right\} \tag{24}$$

where

$$t_m = \begin{cases} \dfrac{x_m - x_{f6}}{x_{f6} - x_{b1}} & x_{f1} < x_m < x_{f6} \\ 1 & x_{b1} \le x_m \le x_{f1} \\ \dfrac{x_{b6} - x_m}{x_{b6} - x_{b1}} & x_{b6} < x_m < x_{b1} \end{cases} \tag{25}$$

$$t_n = \begin{cases} \dfrac{y_n - y_{r6}}{y_{r6} - y_{r1}} & y_{r1} < y_n < y_{r6} \\ 1 & y_{l1} \le y_n \le y_{r1} \\ \dfrac{y_{l6} - y_n}{y_{l6} - y_{l1}} & y_{l6} < y_n < y_{l1} \end{cases} \tag{26}$$

and x_{f1}, x_{b1} and x_{f6}, x_{b6} are the front and back boundaries, y_{r1}, y_{l1} and y_{r6}, y_{l6} are the right and left boundaries of the first and sixth Fresnel zones, respectively. A sample weighting function for the illuminated length is shown in Figure 5.

2.4 VOLTAGE SUMMATION

As discussed above, the voltage summation is carried out over M × N facets falling within an illuminated region which is bounded by the sixth Fresnel zone. The scattered signal is complex and for sampled aperture computations, the scattered voltage is calculated for each of K elements present, each with its own h_1, in effect. The multipath voltage received at the k'th element $V_r(k)$ can be written as:

$$V_r(k) = \sum_{n}^{N} \sum_{m}^{M} w_{mn}(k) \cdot s_{mn}(k) \cdot \Delta V_{mn}(k)\ e^{j\Phi mn(k)} \tag{27}$$

where s_{mn} is a binary shadowing variable, and $\Phi_{mn}(k)$ is the phase difference for reflection from the mn'th facet to the k'th antenna element, given by:

$$\Phi_{mn} = \frac{2\pi}{\lambda} [R_i - R_d]_{mn} + \Phi_r \ . \tag{28}$$

In Eqn. (28), the path difference between indirect and direct signals for the mn'th facet is $[R_i - R_d]_{mn}$, and Φ_r is the reflection phase derived from the complex reflection coefficient. R_i is the path length from transmitter–to–facet–to–receiver element, given by:

$$R_i = R_1 + R_2 \qquad (29)$$
$$= \sqrt{(h_1(k)-z_{mn})^2 + x_m^2 + y_n^2} + \sqrt{(h_2-z_{mn})^2 + (r-x_m)^2 + y_n^2} \quad .$$

If earth curvature is included, R_i is more completely written as:

$$R_i = \sqrt{(h_1(k) - z_{mn} + \Delta(h_1 x))^2 + x_m^2 + y_n^2} + \qquad (30)$$
$$\sqrt{(h_2 - z_{mn} - \Delta(x h_2))^2 + (r-x_m)^2 + y_n^2} \quad .$$

2.4.1 SHADOWING

The binary shadowing variable s_{mn}, introduced above in Equation (27) is more fully defined in this Section. For a given facet of interest it is necessary to check adjacent wavecrests or facets for shadowing, either of the incident signal or the reflected signal, in order to determine whether to include its contribution in the scattered voltage summation. White and Gery [4] derive an index for the number of adjacent wave crests to test based on the maximum wave height of the rough sea and geometrical considerations. This approach is modified to account for the superposition of an arbitrary number of waves with differing physical parameters [2].

In the White Gery approach, for a facet of interest with height z_{mn}, maximum wave height $z_{mn}(max)$ and water wavelength L, n_t adjacent wavecrests are tested toward the transmitter and n_r adjacent wavecrests toward the receiver where

$$n_t = \frac{x_2 \, (\, z_{mn}(max) - z_{mn} \,)}{L \; h_2} \qquad (31)$$

$$n_r = \frac{x_1 \, (\, z_{mn}(max) - z_{mn})}{L \; h_1} \quad . \qquad (32)$$

The height of the lines of sight from the wavecrest under test is evaluated and compared with the adjacent n_r and n_t wavecrests – if the line of sight is lower than any of the wavecrests tested, the contribution of the wavecrest under test is ignored. Since wavecrests follow Rayleigh statistics in the White Gery model, $z_{mn}(\max)$ reduces to $12\sigma\sqrt{2}$ whereas for arbitrary surfaces, $z_{mn}(\max)$ is conservatively taken as the in–phase summation of all contributing waves.

Further modifying the White Gery approach to shadowing, to account for the superposition of sinusoidal waves having a variety of wavelengths, an average or effective wavelength is computed to approximate L in Eqns. (31) and (32). Also, to account for oblique scattering, n_r and n_t wavecrests are tested along the r_1 and r_2 vectors shown in Fig. 2. Adjusting the x coordinate and using the tangent to follow the r_1 and r_2 vectors, the adjacent facet heights are calculated as well as elevation angles with respect to antenna (α_1') and transmitter (α_2'). The two possible shadowing cases are pictured in Figure 6 and it is seen that shadowing occurs when

$$(\alpha_1' < \alpha_1) \text{ and } (\alpha_2' < \alpha_2) \ .$$

A binary variable s_{mn} can thus be written to account for shadowing, as follows:

$$s_{mn} = \begin{cases} 1 & \text{if } \alpha_1 > \alpha_1' \text{ and } \alpha_2 > \alpha_2' \quad \text{(unshadowed)} \\ 0 & \text{otherwise} \qquad\qquad\qquad\quad \text{(shadowed)} \end{cases} \tag{33}$$

2.4.2 COMPLEX REFLECTION COEFFICIENT

A complex reflection coefficient, depending on the polarization of the input signal and varying with grazing angle is required in computing the voltage scattered from a facet. Note that the complex reflection coefficient has been implemented in the current software revision and was not included in previous work [1,2]. Reflection coefficients for vertical (R_0^+) and horizontal (R_0^-) polarizations are given by [3]:

$$R_0^+ = \frac{Y^2\sin\gamma - \sqrt{Y^2 - \cos^2\gamma}}{Y^2\sin\gamma + \sqrt{Y^2 - \cos^2\gamma}} \tag{34}$$

$$R_0^- = \frac{\sin\gamma - \sqrt{Y^2 - \cos^2\gamma}}{\sin\gamma + \sqrt{Y^2 - \cos^2\gamma}} \tag{35}$$

where $\gamma = \alpha_2$ is the grazing angle of the incident signal

$Y = \sqrt{\varepsilon_{rc}/\mu_{rc}}$ is the normalized admittance,

$\mu_{rc} = \mu/\mu_o$ is the relative magnetic permeability,

$\varepsilon_{rc} = \frac{\varepsilon}{\varepsilon_o} + i\ 60\ \lambda\ \sigma$ is the relative complex dielectric constant,

and θ_1, β are defined as above. For the case of sea water, the relative permittivity $\varepsilon/\varepsilon_0 = 80$, and the conductivity $\sigma = 4$ mho/m.

The complex reflection coefficient R_0 can be written as:

$$R_0 = |R_0|\ e^{j\Phi_r} \tag{36}$$

where $|R_0|$ is the magnitude of the reflection coefficient for a smooth earth and Φ_r is the reflection phase. Note that since R_0 is dependent on grazing angle, hence facet position, R_0 is written as R_{mn} in the summation of Equation (27). For the case of curved earth geometry, the reflection coefficient is modified by the divergence factor D_m (derived in the following Section) and becomes:

$$R_{mn} \equiv D_m R_0 = D_m\ |R_0|\ e^{j\Phi_r} \tag{37}$$

2.4.3 DIVERGENCE

A divergence factor D_m is required in computing the voltage scattered from a facet in order to account for earth curvature effects. Curved earth geometry is shown in Figure 3 and derivation of this factor presented in [5]. Variation of the divergence factor with width, i.e., across the illuminated region, is assumed negligible as $(y_l - y_r)$ is small relative to $(x_b - x_f)$. The divergence D_m is given by:

$$D_m = \left[1 + \frac{4\, S_1^2\, S_2\, T}{S\,(1 - S_1^2)\,(1 + T)} \right]^{-1/2} \qquad (38)$$

where

$$T = \left[\frac{h_2}{h_1} \right]^{1/2}$$

$$S = \frac{r}{(2\, a_e\, h_1)^{1/2} + (2\, a_e\, h_2)^{1/2}}$$

$$S_1 = \frac{x_m}{\left[2\, a_e\, h_1 \right]^{1/2}}$$

$$S_2 = \frac{r - x_m}{\left[2\, a_e\, h_2 \right]^{1/2}}$$

For the above, r is the transmitter–receiver separation and a_e is the effective earth's radius (= 8.5×10^6 m). All other parameters are as previously defined.

2.5 FIRST ORDER ANTENNA THEORY

First Order Antenna Theory [6] is applied in the derivation of ΔV_{mn}, the voltage scattered by the mn'th facet to the receiver. Several models were investigated in previous work [2] but the First Order Antenna approach has been recently refined to provide consistent behaviour in describing ocean multipath. Minor modifications to the original First Order approach will be outlined in turn, but the major improvement can be attributed to a more complete treatment of the coordinate rotations required in computing the receiver direction relative to the scattered beam direction. Derivation of this coordinate rotation is presented in Section 2.5.1.

With reference to Figure 2, it can be shown that for transmitted power P_t and a facet at distance r_2 away from the transmitter, the power incident on the facet P_d is given by:

$$P_d = \frac{P_t}{4 \pi r_2^2} \quad . \tag{39}$$

Since the effective facet area is $X \cdot Y \sin\alpha_2$, the received facet power P_{rec} is written as:

$$P_{rec} = \frac{X \cdot Y \sin\alpha_2 \, P_t}{4 \pi r_2^2} \quad , \tag{40}$$

where X, Y are the facet dimensions given by (21), and α_2 is the grazing angle. The power re–radiated by the facet P_{rad} is

$$P_{rad} = \frac{|R|^2 \, X \, Y \sin\alpha_2 \, P_t}{4 \pi r_2^2} \tag{41}$$

where

$|R|$ = modulus of the reflection coefficient

R = $|R| e^{j\Phi}$ is the complex reflection coefficient

Φ = phase angle of the reflection coefficient .

The power density at the receiver P_{dr} is given by:

$$P_{dr} = \frac{P_{rad}}{4 \pi r_1^2} G_p \tag{42}$$

where G_p is the gain of the facet along the facet–receiver line–of–sight. The normalized gain for a rectangular aperture is a two–dimensional sinc function f(u,v) [6], written as:

$$f(u,v) = \frac{\sin\left\{(2\pi/\lambda) \cdot (X \cdot \sin\alpha_2/2) \cdot u\right\}}{(2\pi/\lambda) \cdot (X \cdot \sin\alpha_2/2) \cdot u} \cdot \frac{\sin\left\{(2\pi/\lambda) \cdot (Y/2) \cdot v\right\}}{(2\pi/\lambda) \cdot (Y/2) \cdot v} \tag{43}$$

where u and v are spherical coordinates ($u = \sin\theta \cdot \cos\phi$, $v = \sin\theta \cdot \sin\phi$).

At this point, the facet coordinate system is rotated to coincide with the beam direction, i.e., α_1 and β_1 are expressed in terms of the beam direction coordinate system. In this way the facet gain along the receiver's line–of–sight is calculable.

2.5.1 COORDINATE ROTATION

The following derivation gives a detailed look at the coordinate rotations involved in determining the reflected beam direction, i.e., the vector describing the axis of the multipath beam after reflection from a facet with arbitrary slope and coordinates [7]. With reference to Figures 7(a,b) and 8(a,b), the coordinate rotation is seen to involve 4 steps:

(1) Counter–clockwise rotation by β wrt y axis

$$\underline{R}_y(\beta) = \begin{bmatrix} \cos\beta & 0 & -\sin\beta \\ 0 & 1 & 0 \\ \sin\beta & 0 & \cos\beta \end{bmatrix}$$

(2) Counter–clockwise rotation by α wrt x axis

$$\underline{R}_x(\alpha) = \begin{bmatrix} 1 & 0 & 0 \\ 0 & \cos\alpha & \sin\alpha \\ 0 & -\sin\alpha & \cos\alpha \end{bmatrix}$$

(3) Counter–clockwise rotation by β_2 wrt z axis

$$\underline{R}_z(\beta_2) = \begin{bmatrix} \cos\beta_2 & \sin\beta_2 & 0 \\ -\sin\beta_2 & \cos\beta_2 & 0 \\ 0 & 0 & 1 \end{bmatrix}$$

(4) Counter–clockwise rotation by $(90^\circ - \alpha_2)$ wrt y axis.

$$\underline{R}_y(90-\alpha_2) = \begin{bmatrix} \sin\alpha_2 & 0 & -\cos\alpha_2 \\ 0 & 1 & 0 \\ \cos\alpha_2 & 0 & \sin\alpha_2 \end{bmatrix}$$

The overall rotation matrix $\underline{R}$ is given by the product of these four rotation matrices:

$$\underline{R} = \underline{R}_y(\beta)\, \underline{R}_x(\alpha)\, \underline{R}_z(\beta_2)\, \underline{R}_y(90-\alpha_2) \qquad (44)$$

The matrix $\underline{R}$, in effect, rotates the xyz coordinate system along the beam direction. The x′y′ plane of the facet forms an orthonormal basis for the beam direction, which lies along the z′ axis.

$$\underline{B}' = \underline{R}\,\underline{B}$$

where

$$\underline{B} = \underline{x} + \underline{y} + \underline{z}$$
$$\underline{B}' = \underline{x}' + \underline{y}' + \underline{z}'$$

and

$\underline{x} = x\hat{x}$, $\underline{y} = y\hat{y}$, $\underline{z} = z\hat{z}$, $\hat{x},\hat{y},\hat{z}$ are unit vectors,

$\underline{x}' = x'\hat{x}'$, $\underline{y}' = y'\hat{y}'$, $\underline{z}' = z'\hat{z}'$, $\hat{x}',\hat{y}',\hat{z}'$ are unit vectors.

expresses the new coordinate system in relation to the original coordinate system. Writing the $\underline{B}'$ components with respect to the original coordinate system,

$$\begin{aligned}\underline{x}' = &\left\{ \cos\beta\cdot\sin\alpha_2\cdot\cos\beta_2 - \sin\alpha\cdot\sin\beta\cdot\sin\alpha_2\cdot\sin\beta_2 - \cos\alpha\cdot\sin\beta\cdot\cos\alpha_2 \right\}\hat{x}\\ &+\left\{ \cos\beta\cdot\sin\beta_2 + \sin\alpha\cdot\sin\beta\cdot\cos\beta_2 \right\}\hat{y}\\ &+\left\{ -\cos\beta\cdot\cos\alpha_2\cdot\cos\beta_2 + \sin\alpha\cdot\sin\beta\cdot\cos\alpha_2\cdot\sin\beta_2 - \cos\alpha\cdot\sin\beta\cdot\sin\alpha_2 \right\}\hat{z}\end{aligned}$$

$$\begin{aligned}\underline{y}' = &\left\{ -\cos\alpha\cdot\sin\alpha_2\cdot\sin\beta_2 + \sin\alpha\cdot\cos\alpha_2 \right\}\hat{x}\\ &+\left\{ \cos\alpha\cdot\cos\beta_2 \right\}\hat{y}\\ &+\left\{ \cos\alpha\cdot\cos\alpha_2\cdot\sin\beta_2 + \sin\alpha\cdot\sin\alpha_2 \right\}\hat{z}\end{aligned}$$

$$\begin{aligned}\underline{z}' = &\left\{ \sin\beta\cdot\sin\alpha_2\cdot\cos\beta_2 + \sin\alpha\cdot\cos\beta\cdot\sin\alpha_2\cdot\sin\beta_2 + \cos\alpha\cdot\cos\beta\cdot\cos\alpha_2 \right\}\hat{x}\\ &+\left\{ \sin\beta\cdot\sin\beta_2 - \sin\alpha\cdot\cos\beta\cdot\cos\beta_2 \right\}\hat{y}\\ &+\left\{ -\sin\beta\cdot\cos\alpha_2\cdot\cos\beta_2 - \sin\alpha\cdot\cos\beta\cdot\cos\alpha_2\cdot\sin\beta_2 + \cos\alpha\cdot\cos\beta\cdot\sin\alpha_2 \right\}\hat{z}\end{aligned}$$

Direction cosines for the facet–receiver vector can be written as:

$$x_1 = \cos\alpha_1\cdot\cos\beta_1\cdot\hat{x}$$
$$y_1 = \cos\alpha_1\cdot\sin\beta_1\cdot\hat{y}$$
$$z_1 = \sin\alpha_1\cdot\hat{z}$$

Taking the dot product of these direction cosines with the components of the beam vector gives the new direction cosines with respect to the rotated coordinate system. These become the u′,v′ arguments to the sinc function in determining the scattered voltage:

$$\begin{aligned} u' = {} & \cos\alpha_1 \cdot \cos\beta_1 \cdot \left\{ \cos\beta \cdot \sin\alpha_2 \cdot \cos\beta_2 - \sin\alpha \cdot \sin\beta \cdot \sin\alpha_2 \cdot \sin\beta_2 \right. \\ & \left. - \cos\alpha \cdot \sin\beta \cdot \cos\alpha_2 \right\} - \cos\alpha_1 \cdot \sin\beta_1 \cdot \left\{ \cos\beta \cdot \sin\beta_2 + \sin\alpha \cdot \sin\beta \cdot \cos\beta_2 \right\} \\ & + \sin\alpha_1 \cdot \left\{ -\cos\beta \cdot \cos\alpha_2 \cdot \cos\beta_2 + \sin\alpha \cdot \sin\beta \cdot \cos\alpha_2 \cdot \sin\beta_2 - \cos\alpha \cdot \sin\beta \cdot \sin\alpha_2 \right\} \end{aligned} \tag{45}$$

$$\begin{aligned} v' = {} & \cos\alpha_1 \cdot \cos\beta_1 \cdot \left\{ -\cos\alpha \cdot \sin\alpha_2 \cdot \sin\beta_2 + \sin\alpha \cdot \cos\alpha_2 \right\} \\ & + \cos\alpha_1 \cdot \sin\beta_1 \cdot \left\{ \cos\alpha \cdot \cos\beta_2 \right\} \\ & + \sin\alpha_1 \cdot \left\{ \cos\alpha \cdot \cos\alpha_2 \cdot \sin\beta_2 + \sin\alpha \cdot \sin\alpha_2 \right\} \end{aligned} \tag{46}$$

Note that for the smooth sea case, $\alpha = \beta = 0$, thus

$$\cos\alpha = \cos\beta = 1$$
$$\sin\alpha = \sin\beta = 0$$

and u′, v′ reduce to:

$$u' = \cos\alpha_1 \cdot \cos\beta_1 \cdot \sin\alpha_2 \cdot \cos\beta_2 + \cos\alpha_1 \cdot \sin\beta_1 \cdot \sin\beta_2 - \sin\alpha_1 \cdot \cos\alpha_2 \cdot \cos\beta_2$$
$$v' = -\cos\alpha_1 \cdot \cos\beta_1 \cdot \sin\alpha_2 \cdot \sin\beta_2 + \cos\alpha_1 \cdot \sin\beta_1 \cdot \cos\beta_2 + \sin\alpha_1 \cdot \cos\alpha_2 \cdot \sin\beta_2 \ .$$

2.5.2 RECEIVED VOLTAGE

The gain of the facet–to–receiver line–of–sight can be expressed as [6]

$$G_p = D_p \cdot [f(u',v')]^2$$

where $D_p = \dfrac{4\pi}{\Theta_B \Psi_B}$ = maximum directivity gain of the facet.

Since the beamwidths $\Theta_B = \dfrac{0.886\ \lambda}{X \sin\alpha_2}$ and $\Psi_B = \dfrac{0.886\ \lambda}{Y}$,

$$D_p = \frac{4 \cdot \pi \cdot X \cdot Y \cdot \sin\alpha_2}{(0.886\ \lambda)^2} \ ,$$

and thus

$$G_p = \frac{4\pi XY \cdot \sin\alpha_2}{(0.886\lambda)^2} \cdot \left[\frac{\sin\left\{(2\pi/\lambda)\cdot\frac{(X\cdot\sin\alpha_2)}{2}\cdot u'\right\}}{(2\pi/\lambda)\cdot(X\cdot\sin\alpha_2/2)\cdot u'}\right] \cdot \left[\frac{\sin\left\{(2\pi/\lambda)\cdot(Y/2)\cdot v'\right\}}{(2\pi/\lambda)\cdot(Y/2)\cdot v'}\right]$$

The power ΔP arriving at the antenna is the product of the incident power density P_{dr} (42) and the capture area A_r effective in the direction of arrival, i.e.,

$$\Delta P = A_r \cdot P_{dr} = \frac{\lambda^2}{4\pi} \cdot G_p \cdot P_{dr}$$

Substituting for G_p and P_{dr} gives:

$$\Delta P = \frac{\lambda^2}{4\pi} \cdot \frac{|R|^2 XY \sin\alpha_2 \, P_t}{(4\pi)^2 r_1^2 r_2^2} \cdot \frac{4\pi X Y \sin\alpha_2}{(0.886\lambda)^2} \cdot \left[\frac{\sin\left\{(2\pi/\lambda)\cdot(X\cdot\sin\alpha_2/2)\cdot u'\right\}}{(2\pi/\lambda)\cdot(X\cdot\sin\alpha_2/2)\cdot u'}\right]^2 \cdot \left[\frac{\sin\left\{(2\pi/\lambda)\cdot(Y/2)\cdot v'\right\}}{(2\pi/\lambda)\cdot(Y/2)\cdot v'}\right]^2 . \quad (47)$$

If the antenna is matched to a 1-ohm load, the received voltage is:

$$\Delta V = \sqrt{\Delta P} \ ,$$

therefore the voltage increment due to reflection from the mn'th facet is

$$\Delta V_{mn} = \frac{|R|}{0.886\cdot 4\pi} \frac{XY \sin\alpha_2 \sqrt{P_t}}{r_1 r_2} \left[\frac{\sin\left\{(2\pi/\lambda)\cdot(X\cdot\sin\alpha_2/2)\cdot u'\right\}}{(2\pi/\lambda)\cdot(X\cdot\sin\alpha_2/2)\cdot u'}\right] \left[\frac{\sin\left\{(2\pi/\lambda)\cdot(Y/2)\cdot v'\right\}}{(2\pi/\lambda)\cdot(Y/2)\cdot v'}\right] \quad (48)$$

where u' and v' are defined in Eqns. (45) and (46).

3 DESCRIPTION OF SIMULATION SOFTWARE

Software functionality is described in the block diagram of Figure 9. Geometrical parameters such as transmitter and receiver heights, range, antenna aperture size and number of elements are user–selectable, and either curved or flat earth geometries can be employed. Sea state parameters such as the desired number of snapshots, the number of waves for superposition, as well as each wave's height, phase shift, wavelength, propagation angle are also user inputs, allowing for arbitrarily rough surface or sea swell simulation. The grid size for the illuminated region is also user–defined as well as transmission properties such as power transmitted, EM wavelength, and polarization.

The program computes scattered voltages on a strip–by–strip basis (i.e., y_n constant, x_m varies) for each element, allowing the display of either Cornu strip voltage for a particular strip and element, or a surface plot of the scattered voltage from all facets for an individual element. The latter representation is particularly useful for examining edge effects and gauging the effectiveness of weighting. The total multipath signal for each antenna element is arrived at by complex summation of the scattering contributions from all illuminated facets. This multipath signal is then combined with the calculated direct signal and the total received signal across the array is determined. The user then has the choice of displaying amplitude, phase, real or imaginary parts for either the direct–only, indirect–only (multipath), or total signals.

4 SIMULATION STUDIES

Verification of the sea swell modeling software begins by examining the receiver interference pattern under zero sea state conditions initially. Comparison of obtained interference pattern null spacings and positions versus theory provide a good overall test of model accuracy. Following this, rough sea surfaces are introduced and the effect of sea state on the interference pattern is shown. The effect of varying grid area on the interference pattern is also illustrated and the problem of defining an adequate facet size is addressed.

P148367.PDF [Page: 26 of 80]

4.1 INTERFERENCE PATTERN NULL SPACING

For constant transmitter–receiver separation, the interference pattern is obtained by computing the complex voltage sum of direct and total multipath signals along the receiver aperture. This interference pattern will, in general, illustrate constructive interference denoted by peaks and destructive interference indicated by nulls. An odd multiple of π in the phase difference between direct and indirect signals will produce a null while an even multiple of π results in a peak.

The combined phase of the multipath signal can be expressed in terms of an approximate path difference [5], given by:

$$\phi = -k\Delta R + \phi_r$$

where

$$\Delta R = \frac{2h_1h_2}{r}$$

is the approximate path difference obtained for a simple flat earth geometrical reflection model, k is the wavenumber ($2\pi/\lambda$), h_1 and h_2 are the heights of the receiver and transmitter, respectively, r is the horizontal separation between the receiver and transmitter, and ϕ_r is the reflection phase. For a flat sea surface, ϕ_r is approximately $-\pi$ and the null positions can be determined by assigning the combined multipath phase to any odd multiple of π, giving,

$$h_{null} = \frac{\lambda R}{2h_2} \cdot n$$

where the factor $\lambda R/(2h_2)$ gives the spacing between any two adjacent nulls and n is an integer.

Alternatively, the null separation S_{mm} is given by [5]:

$$S_{mm} = \frac{\lambda}{2 \sin \alpha} \tag{49a}$$

where

$\alpha = \alpha_d + |\alpha_i|$

α_d = direct signal elevation angle

α_i = indirect signal elevation angle (specular).

Figures 10(a) and 10(b) show the interference pattern obtained for a source at 20 m height, 5 km range, and a 128–element receive antenna with 20 m aperture, centered at a height of 20 m. Zero sea state, flat earth geometry is

P148367.PDF [Page: 27 of 80]

used for the simulation and M×N = 1000×30 is assumed to provide adequate grid resolution. The interference pattern of Figure 10(a) shows uneven null spacing and was computed based on path length differences with respect to the centre of the receiver array. Figure 10(b) was computed by taking path length differences with respect to the individual antenna elements and exhibits equal null spacing of approximately 4.0 m, giving excellent agreement with the theoretical spacing predicted by Eqn. (49a).

4.2 INTERFERENCE PATTERN NULL LOCATION

As derived in [5], interference pattern null heights occur when the total phase difference is a multiple of π. It can be shown that null heights s_m are described by:

$$s_m = \frac{(2m + 2l + 1)\pi - \chi_P^T}{\frac{2\pi}{\lambda}(\sin\alpha_d - \sin\alpha_i)} \qquad (49b)$$

where $m = ..., -2, -1, 0, 1, 2, ...$

and χ_P^T = total phase difference
= phase due to path length difference + reflection phase .

Using Equation (49b) and the same range parameters as in Section 4.1, nulls are predicted to occur at 12.0, 16.0, 20.0, 24.0, and 28.0 m. Simulated result shown in Figures 11(a) and (b) are for flat and curved earth geometries, respectively, and show excellent agreement with theory. This further confirms correct operation of the current software revision. Previous revisions had a factor of j omitted during the scattered voltage derivation, leading to a phase shift of +90o and hence inconsistent null locations. This is readily apparent when the result of Figure 10(b) is compared with that of Figure 11(a).

4.3 EFFECT OF VARYING GRID RESOLUTION

A qualitative approach to deriving a measure of the grid area required for adequate null resolution is outlined in this Section. Range, target and receiver parameters, and sea state are fixed while the number of x and y grid points are

varied independently. For the following simulation results H_1=10 m, H_2=20 m, range= 2 km, and an 6 m array consisting of 32 elements is used, similar to the measurement parameters for the Lake Huron trials. Note that the following results were obtained using previous software revision so null position data is inaccurate – the current goal is to illustrate the qualitative approach to defining null resolution.

Plotting null positions versus the number of x grid points (M) for a fixed number of y grid points (N=20, initially) as in Figure 12(a) shows that the antenna interference pattern better resolves the nulls as M increases, stabilizing for M>30. The illuminated length is 1050.8 m for the given range parameters, hence M=30 corresponds to a facet length of 35.0 m. Fixing M=500 and repeating the above for varying N gives the results of Fig 12(b). In this case, null resolution stabilizes for N>20, and since the illuminated width is 18.8 m, this corresponds to a facet width of .94 m. Since these results are for zero sea state, the required facet area will be much greater than for rough seas. Once the facet area required to obtain adequate null resolution is determined, the number of facets can be scaled according to the dimensions of the illuminated region in order to provided the desired facet area.

A more quantitative approach to the testing of shadowing and the issue of adequate grid resolution may be obtained by adopting a sampling theorem analysis of the sea swell surface. A sampling criterion based on wave heights and water wavelengths may be derived and aliasing considerations would then dictate the required grid resolution, i.e., the maximum "frequency" content of fluctuations of the sea surface would determine the necessary physical sampling, thus grid resolution. If such a sampling criterion could be defined, shadowing would also be unambiguous since the surface would be completely characterized, given the satisfaction of the sampling criterion.

4.4 ROUGH SEA

The following simulations are for varying sea state while range parameters and grid resolution are held constant. Geometrical parameters are: $h_1 = h_2$ = 20 m, range = 5 km; antenna aperture = 20 m; number of receiver elements = 128; and M×N = 1000×30. The water wavelength is fixed at 100 m

and wave heights of 0.0, .25, .50, and .75 are selected. Received signal amplitude results are pictured in Figures 11(a), and 13(a,b,c) and it is seen that as sea state increases, null resolution decreases, i.e., the interference pattern degrades. The most important thing to note in these results is that the null location remains constant despite the degradation of the interference pattern. This implies consistent behavior of the current revision of sea swell modeling software.

5 CORRELATION HEIGHT ANALYSIS OF EXPERIMENTAL RESULTS

5.1 INTRODUCTION

Correlation Height Analysis (CHA) refers to a superresolution algorithm designed for use with tracking radars which, under normal conditions, provides a considerable improvement in the accuracy of angle–of–arrival estimates for low–angle targets. The technique uses a deterministic model to simulate multipath propagation and a family of target heights are derived by the cross–correlating theoretical data obtained from the simulated model with measured data. By using multiple–frequency data, the true target height can be identified.

This chapter describes results obtained from the analysis of Lake Huron data using the CHA technique. Section 5.2 gives a description of the data measurement procedures while in Section 5.3, calibration procedures are addressed. CHA results are be presented along with discussion in Section 5.4.

5.2 LAKE HURON DATA MEASUREMENT

In late October 1987, a series of experiments were performed on the west coast of the Bruce Peninsula close to Tobermory, Ontario, overlooking Lake Huron. This particular location was chosen because of the high sea states caused by a combination of westerly winds, the shallow water offshore, and the long fetch across Lake Huron. The experiments were designed to acquire data suitable for (1) evaluating the performance of high–resolution spectrum estimation and adaptive beamforming techniques, and (2) investigating the correlation between the characteristics of the direct and multipath signals with meteorological and sea state conditions. Fig. 14 shows the measurement area, with R indicating the location of the receiver and T the transmitter. Fig. 14 also illustrates the water

depth along the transmission path. The greatest depth along the path is 6.5 fathoms or 12 meters. A multi–parameter adaptive radar system (MARS) [8], which was developed at the Communications Research Laboratory, McMaster University, was used to collect data under a variety of meteorological and water surface conditions.

5.2.1 MULTI–PARAMETER ADAPTIVE RADAR SYSTEM (MARS)

The MARS is a bistatic radar, consisting of a transmitter, a 32–element sampled aperture antenna, and a data acquisition system. The antenna array is depicted in Fig. 15. The transmitter was sited at a distance of 4610 meters from the receiving antenna. In Fig. 16, the vertical plane view gives the geometry of the experimental setup. System specifications are summarized as follows:

Specifications of the Measurement System
(MARS) used in the Lake Huron Experiments

Transmitter
- 100 mV CW into 22 dB horn(s)
- simultaneous dual frequencies
- horizontal or vertical polarization
- adjustable transmitter height

Antenna Array
- 32–element linear array
- 1.82 meter aperture, 0.05715 meter inter–element spacing
- 10 dB H–polarized horns
- machined to ± 0.1 mm machine tolerance
- multi–frequencies: 8.0 to 12.4 GHz in 30 MHz steps

Receivers
- coherent modulation, with frequency stability to 10^{-12}
- accuracy of 0.1 dB and 1^0
- 0.1 Hz Doppler resolution
- 1 Hz to 2 KHz sampling rate
- 6–term error model

Transmitter: As shown in Fig. 17, the microwave source was produced by phase locking to a highly stable 5 MHz crystal oscillator which was operating at a constant temperature. A travelling wave tube amplifier (TWTA) with a maximum gain of 40 dB was used to amplify the output of the microwave source. The output signal from the TWTA was fed through the switch into one of the two 22–dB horns mounted on the tower through a coaxial cable and, if required, into another 22–dB horn which was installed just above the water surface via an elliptical waveguide. The height of the carriage on which the horns were mounted could be varied through a height interval of 16 meters by a servo–motor. The entire transmitter system could be operated either from the local control panel or from the main computer at the receiver site via radio link.

Receiver: The receiver system consists of the array and the receiver circuitry. The array had a 1.82 meter aperture across which the 32 10–dB, horizontally polarized horns were uniformly placed to form a linear array. The individual array elements were precisely aligned and uniformly distributed to within 0.0001 meter to minimize errors due to misalignment and uneven spacing between elements. Each horn was connected to a coherent receiver which has two frequency channels, the fix–frequency channel, the agile–frequency channel. Since these two channels were identical, only one channel is shown in Fig. 18 for simplicity. The RF and IF local oscillators and the RF testing signal generator were shared by all the receivers. In the receivers, transmission line lengths and component characteristics had been carefully matched to ensure nearly identical performance. Immediately behind each element, the test channel insertion couplers, the RF mixers and the IF amplifiers were connected and included within the antenna enclosure which was mounted at the top of the receiver tower. The rest of the system was installed in the equipment tent at the base of the tower. An RF signal via the antenna or the test channel insertion coupler was mixed with the RF local oscillator to obtain a 45 MHz IF signal which was then amplified by the IF amplifier. The output of the IF amplifier was mixed with the IF local oscillator in the in–phase (I) and quadrature (Q) channels to produce a baseband signal. The phase of the IF local oscillator for the Q channel is advanced by $\pi/2$. The baseband signal was amplified and low–pass filtered to obtain the field aperture distribution which was recorded by the data acquisition system.

Data Acquisition: The data acquisition system consisted of the samplers, multiplexers, A/D converters, direct memory access (DMA) controller, and random access memory (RAM), as indicated in Fig. 19. After being low–pass filtered, the baseband signals were sampled by the sample–and–hold circuits whose sampling rate was controllable with a maximum value of 2 KHz. The sampled signals from the 32 channels were then multiplexed and digitized by the A/D converters with 12–bit precision. The digitized outputs were stored through the DMA controller and via the computer bus into RAM. From one measurement to another, the contents of the RAM were stored onto hard disk and backed up with magnetic tapes to make room in RAM for the next run.

Computer Control: The main control of the system was provided by the PC–AT model microcomputer at the receiver site. Data collection could be fully automatated and carried out with minimum human intervention. An operator need only feed a set of parameters which defined the physical conditions of the trial into the computer. The computer accordingly adjusted (1) the frequency of the RF oscillator for the agile channels, (2) the gain of the IF amplifiers, (3) the bandwidth of the low–pass filters in the I and Q channels, and (4) the sampling rate of the samplers. It also sent out commands via the radio link to control the operation of the transmitter. The radio link was established with a pair of modems. At the transmitter site, a PC–XT model microcomputer received the control commands and accordingly adjusted (1) the transmission frequency of the agile channel, (2) the gain of the TWTA, and (3) the height of the carriage. One of the horns mounted on the carriage was switched on to transmit with the required polarization.

Data Format: For the Lake Huron trials, data was taken at a sampling rate of 62.5 snapshots/second, corresponding to eight sample points per cycle at baseband frequency. Due to the technical aspects of the array antenna, as it was designed, frequency switching between snapshots is impractical and hence the way that data were collected was limited to switching agile frequency between n number of snapshots. That is to say, n number of snapshots at both fixed frequency and at a particular agile frequency were taken and stored and then the agile frequency was changed to a desired value before the next n number of snapshots were taken and stored. The height interval over which the beacon carriage travelled was from 2.7 m to 18.4 m above water level. The angular

separation of the direct and indirect signals observed at the center of the receiving array antenna is a function of the transmitter height. Fig. 20 depicts the relationship between the separation and the transmitter height.

5.3 CALIBRATION PROCEDURES

The collected data must be calibrated because measurement errors were inevitably introduced into the data due to (1) direct current (dc) offsets in the I and Q channels, (2) differences in the gain and phase characteristics of individual receivers, and (3) discrepancies in the test and local oscillator signals supplied to the receivers. Two procedures were carried out in processing the data to recognize the measurement errors: IQ calibration and far–field calibration.

5.3.1 IQ CALIBRATION

The IQ calibration procedure is designed to measure the gain and phase characteristics of the individual channels on the IF and the baseband stages using the channel model depicted in Fig. 21. The gains in both channel I and channel Q are normalized with respect to that of channel I. Therefore, the gain in channel I is unity and the gain in channel Q is G_q. θ_q represents the relative phase error in channel Q. The dc offsets in both channels are DC_i and DC_q. If the input is an IF signal of the form $Ae^{j\alpha}$, the outputs of both channels are expected to be

$$I = A\cos(\alpha) \tag{50}$$

and

$$Q = A\sin(\alpha) \tag{51}$$

Because of the gain and phase errors and dc offsets in the channels, the actual outputs are instead

$$I' = A\cos(\alpha) + DC_i \tag{52}$$

and

$$Q' = A\,G_q\sin(\alpha-\theta_q) + DC_q \tag{53}$$

Solving for $\cos(\alpha)$ and $\sin(\alpha)$ in Eq.(52) and (53) and substituting into Eq.(50)

and (51), the true in–phase and quadrature–phase components of the signal are obtained,

$$I = I' - DC_i \tag{54}$$

and

$$Q = \frac{1}{\cos(\theta_q)} \left[\frac{Q' - DC_q}{G_q} + I \sin(\theta_q) \right] \tag{55}$$

The parameters DC_i , DC_q , G_q , and θ_q , referred to as IQ calibration coefficients, are determined for each of the receivers.

DC_i and DC_q can be easily determined as follows:

$$DC_i = \frac{1}{N} \sum_{n=1}^{N} I'(n) \tag{56}$$

$$DC_q = \frac{1}{N} \sum_{n=1}^{N} Q'(n) \tag{57}$$

where N is the number of samples and I' and Q' are the temporal data in the corresponding channel.

G_q and θ_q was measured by injecting a test signal whose frequency is offset by a small amount Δf (voltage controlled oscillator frequency offset) so that a baseband signal was produced at Δf Hz. Any imbalance in gain and phase would create an image response at $-\Delta f$ and hence G_q and θ_q could be determined as follows. Let

$$S'(n) = I'(n) + jQ'(n) \tag{58}$$

where
$$I'(n) = A\cos(\Delta\omega nT) + DC_i$$
$$Q'(n) = AG_q\sin(\Delta\omega nT - \theta_q) + DC_q$$
$$\Delta\omega = 2\pi\Delta f$$

The discrete Fourier Transform (DFT) of S'(n), evaluated at $\Delta\omega$, is given as

$$F\{S'(n)\}\Big|_{\omega = \Delta\omega} = \left[\sum_{n=0}^{N-1} S'(n)e^{-j\omega nT} \right] \Big|_{\omega = \Delta\omega}$$

$$= \frac{N A}{2} (1 + G_q \cos\theta_q - jG_q \sin\theta_q) \qquad (59)$$

where $F\{\cdot\}$ denotes the DFT. Similarly, the DFT of S' evaluated at $-\Delta\omega$ is

$$F\{S'(n)\}\Big|_{\omega = -\Delta\omega} = \left[\sum_{n=0}^{N-1} S'(n)e^{-j\omega nT} \right] \Big|_{\omega = -\Delta\omega}$$

$$= \frac{NA}{2} (1 - G_q \cos\theta_q - jG_q \sin\theta_q) \qquad (60)$$

Solving Eqs. (59) and (60) gives the parameters G_q and θ_q of a channel. By repeating the procedures for all 32 elements, calibration coefficients for each frequency channel can be obtained and the measured data can be corrected with Eq. (54) and (55).

5.3.2 FAR–FIELD CALIBRATION

Although the IQ calibration may eliminate the gain and phase errors of the individual channels, it does not measure the relative performance of the receivers to the required accuracy since the test and local oscillator signals applied to the receivers may not be necessarily identical, due to the nature of the distribution network. Therefore, far–field calibration procedure is designed to accurately characterize the front end components which are not covered by the IQ calibration. The technique is uses a far field source to provide uniform aperture distribution as a basis for evaluating the relative parameters. A 22–dB horn was connected to the transmitter and placed about a foot above the water surface to simulate a far field source. The geometry of the far–field calibration setup is given in Fig. 22. Although the multipath phenomenon might still exist, the return is modeled as a single plane wave because the separation between the source and the image was much smaller than could be resolved.

In the ideal situation, because a plane wave is impinging upon the array, the output amplitude of each element is the same whilst the phase is linearly progressive. Due to the imbalance between elements, errors in amplitude and phase will be introduced into the output. To estimate these errors, elemental outputs are normalized with respect to a reference output, say the output of element 0. In addition, since each channel is assumed to have independent zero–mean Gaussian gain and phase noise, temporal ensemble averaging over a time interval N is used to reduce random noise effects. Thus the far–field calibration coefficient $A_{ff}e^{\phi_{ff}}$ for the k'th element is given as

$$A_{ff,k} = \frac{1}{N} \sum_{n=1}^{N} \frac{A_{m,k}(n)}{A_{ref,k}(n)} \tag{61}$$

$$\phi_{ff,k} = \frac{1}{N} \sum_{n=1}^{N} [\phi_{m,k}(n) - \phi_{ref,k}(n)] \tag{62}$$

where the subscript m implies the measured outputs from a far–field source and subscript ref the reference output. With these calibration coefficients, the measured multipath data at the output of a receiver, $Ae^{j\phi}$ can be corrected as follows

$$A_c\, e^{j\phi_c} = \frac{A\, e^{j\phi}}{A_{ff} e^{j\phi_{ff}}} \tag{63}$$

where the subscript c implies the corrected values.

5.4 EXPERIMENTAL RESULTS

5.4.1 ALIAS TRACKS

A family of target tracks can be derived by cross–correlating the measured data with simulated data. In reference [9], an equation is given to describe the behavior of the alias tracks, namely

$$\Delta H_k = (k-k_T)\cdot\Delta H\cdot\left\{ \frac{\Delta f}{f} + \frac{\Delta z_1}{z_1} + \frac{\partial J}{\partial z_1}\cdot\frac{\Delta z_1}{J}\right\}\cdot r \tag{64}$$

P148367.PDF [Page: 37 of 80]

where $(k-k_T)$ identifies the order of the track relative to the true track number k_T, and

$$\Delta H = \frac{\lambda}{2 z_1 J},$$

$\frac{\Delta f}{f}$ = the relative change in the radar frequency, f being the average frequency,

$\frac{\Delta z_1}{z_1}$ = the relative change in the antenna height,

$\frac{\partial J}{\partial z_1} \cdot \frac{\Delta z}{J}$ = a quantity which only becomes significant for very low target heights, and

J = curved earth correction factor.

Since in our measurements the height of the receiving antenna was fixed, the term z_1 vanishes and hence Eq.(64) becomes

$$\Delta H_k = (k-k_T) \cdot \Delta H \cdot \frac{\Delta f}{f} \cdot r$$

$$= (k-k_T) \cdot \frac{\lambda}{2 z_1 J} \cdot \frac{\Delta f}{f} \cdot r$$

$$= (k-k_T) \cdot \frac{r \cdot c}{2 z_1 J} \cdot \frac{\Delta f}{f^2} \quad . \tag{65}$$

It is clear that ΔH_k is a linear function of Δf if f is kept fixed. As Δf increases, ΔH_k increases linearly. On the other hand, if Δf is kept constant, ΔH_k is an inverse quadratic function of f. More generally, ΔH_k can be said to be a function of the combination of Δf and f, i.e.,

$$\Delta H_k = F \ (\Delta f, \ f) \tag{66}$$

which describes a three–dimension surface that reflects the behavior of ΔH_k when both Δf and f are changed, as depicted in Fig. 23. In our case, where there is a fixed–frequency channel and an agile–frequency channel, both Δf and f change if the frequency in the agile channel shifts from one value to another. Therefore, the behavior of the alias tracks is irregular. Fig. 24 displays a group of alias tracks corresponding to a beacon height of 18.45 m. In Fig. 24, it can be

observed that ΔH_1 appears to be the same within the frequency range from 8.0 GHz to 10.0 GHz. Since ΔH_k is used as a criterion for identifying the true track, an ambiguity may arise if the radar frequencies in such a range are used. Similar situations can also be observed in Fig. 25 and Fig. 26. Therefore, in order to avoid this ambiguity, Δf needs to be set sufficiently large.

5.4.2 CHA RESULTS

The CHA results to be presented are based on real multipath data obtained from measurement trials performed on Lake Huron. The roughness of the water surface for this data was about 1.5 m to 2.0 m in terms of wave heights. In processing this data, normal propagation conditions were assumed. In other words, the effective earth radius factor κ was set to be 4/3. Such a value was taken because not enough atmospheric data was available for estimating the index of refractivity. Moreover, all results given here were obtained from the data sets sampled simultaneously from the two frequency channels because the snapshots from both frequency channels were taken under the same propagation and environmental conditions.

Results are shown in Figs. 27 and 28. These were obtained on a single–snapshot basis, i.e., each estimated height resulted from one snapshot. For comparison, we tabulate the statistical parameters of the results in Table 5–1. The angular separation of the direct and indirect signals is given in terms of antenna beamwidth. The beamwidth shown in Fig. 29 is a function of the centre frequency which is the average of the two frequencies used in the CHA processing. In Fig. 27, both curves are for a transmitter height of 18.45 m above water level. However, the angular separations in terms of beamwidth were different since the agile frequency in each case was different. To be specific, the agile frequency was 11.92 GHz for Plot 1 and 8.02 GHz for Plot 2.

Biases and variances were observed in all results. These biases and variances tend to increase as the separation of the direct and indirect signals decreases. Although there were many factors that might contribute to the bias and variance, it is certain that the tilt of the antenna array and its vibration due to strong wind were the two main factors.

P148367.PDF [Page: 39 of 80]

An outstanding advantage of the CHA algorithm can be observed from the comparison of the CHA results with the results obtained from an eigen–based spectral analysis technique called the Principal Eigenvector Gram–Schmid (PEGS) method [10]. The angle–of–arrival (AOA) results given in Fig. 30, which correspond to the case where the transmitter was at 9.53 m above water level and the angular separation was 30% BW, indicate that the PEGS technique failed to resolve the direct and indirect signals. On the other hand, CHA was successful in resolving the target from its image even though the angular separation was one–tenth of a beamwidth. That is, the CHA algorithm offers higher resolvability under the same conditions.

6 CONCLUSIONS AND FUTURE WORK

The report presented a summary of previous theory behind the sea swell model as well as modifications to the theory which resulted in the functionality of the current revision of modeling software. Preliminary results obtained using the simulation software were presented to confirm proper operation and compared with theoretical results where possible. Excellent agreement between model and theory was observed.

In the second part of the report, the application of Correlation Height Analysis to real data obtained during the Lake Huron measurement trials was presented. The experimental setup was described in terms of equipment and range parameters, calibration procedures were outlined, and CHA analysis results were included. The superior performance of CHA with respect to another estimation algorithm was demonstrated.

At this point, intensive simulation studies using the sea swell software model may be carried out. The goal of comparing simulated versus experimental data should be kept in mind, toward validation of the software model and derivation of a correction factor for the CHA algorithm. The only way to validate the model is by comparison with real data and the recently–performed Lake Ontario trials should provide the necessary data base since sea state data is available through the Canada Centre for Inland Waters. Future expansion of the modeling software may include the integration of propagation effects for more comprehensive performance.

P148367.PDF [Page: 40 of 80]

7 REFERENCES

1. J. Litva, "On scattering of electromagnetic waves from sea swells", CRL Report No. 175, December 1986.

2. P. Bauman and J. Litva, "Modeling and analysis of the effect of sea swell on radar low angle tracking performance", CRL Report No. 193, June 1988.

3. P. Beckmann and A. Spizzichino, The Scattering of Electromagnetic Waves From Rough Surfaces, Artech House Inc., Norwood MA, 1987.

4. White, W.D. and S.W. Gery, "Final report on low angle radar study", AIL Report No. 4251–TR1, Nov. 1969.

5. J. Litva and P. Bauman, "Studies of correlation between meteorological and low–level radar angle–of–arrival measurements", CRL Report No. 174, Nov. 1986

6. Balanis, C.A., Antenna Theory Analysis and Design, Harper & Row, New York, 1982.

7. Arfken, Mathematical Methods for Physicists, Artech House.

8. S. Haykin and V. Kezys, "Multi–parameter Adaptive Radar System (MARS)," 30th Midwest Symposium on Circuits and Systems.

9. John Litva, "A New Low–Angle Tracking Technique," CRC Report No. 1335, May 1980.

10. W. F. Gabriel, "A High–Resolution Target–Tracking Concept Using Spectral Estimation Techniques," NRL Report 8797, May 31, 1984.

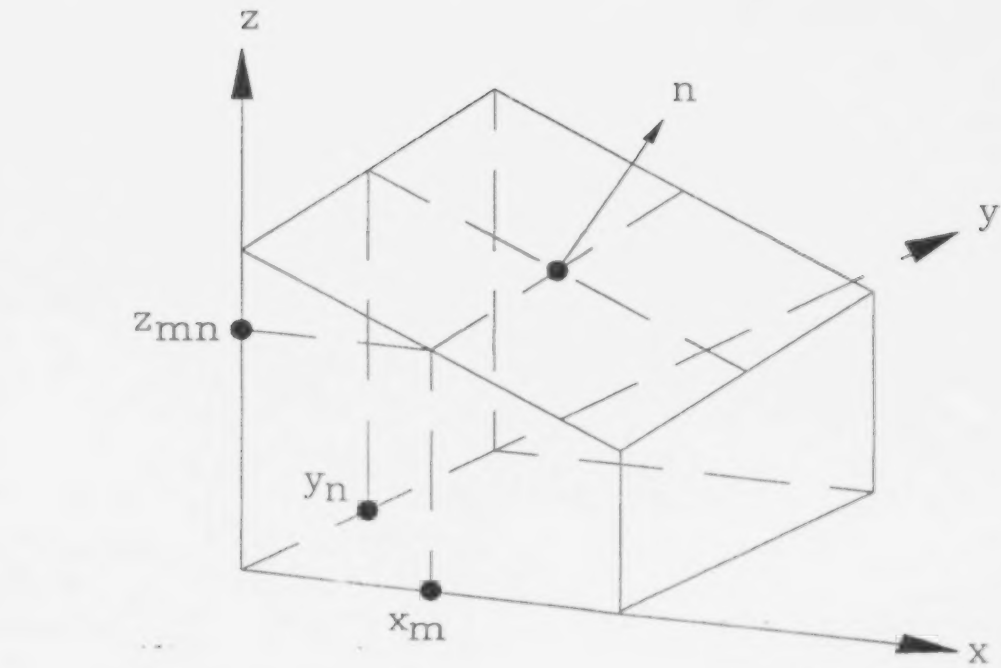

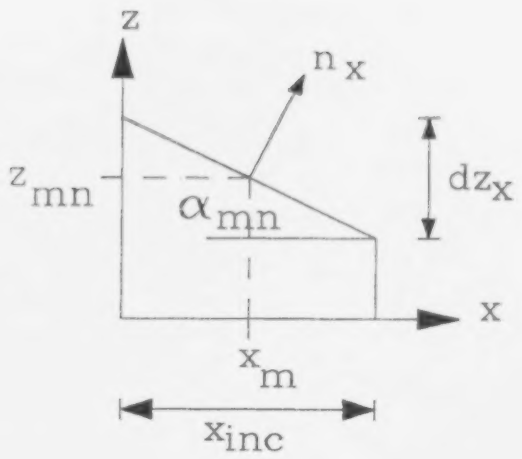

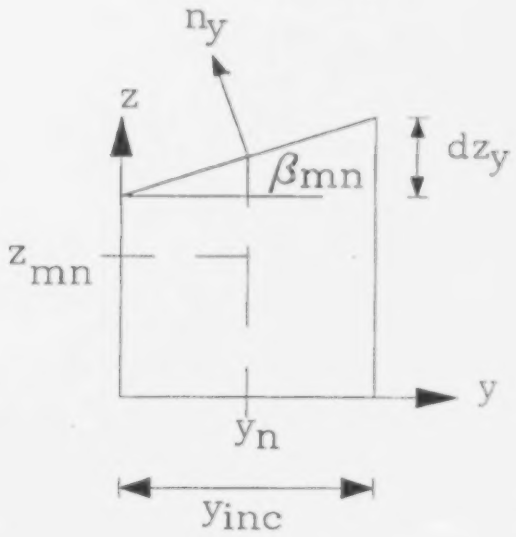

$$\alpha_{mn} = \tan^{-1}\left[dz/dx = \frac{dz_x}{xinc}\right] \qquad \beta_{mn} = \tan^{-1}\left[dz/dy = \frac{dz_y}{yinc}\right]$$

Figure 1: Sea swell facet geometry and slopes.

P148367.PDF [Page: 42 of 80]

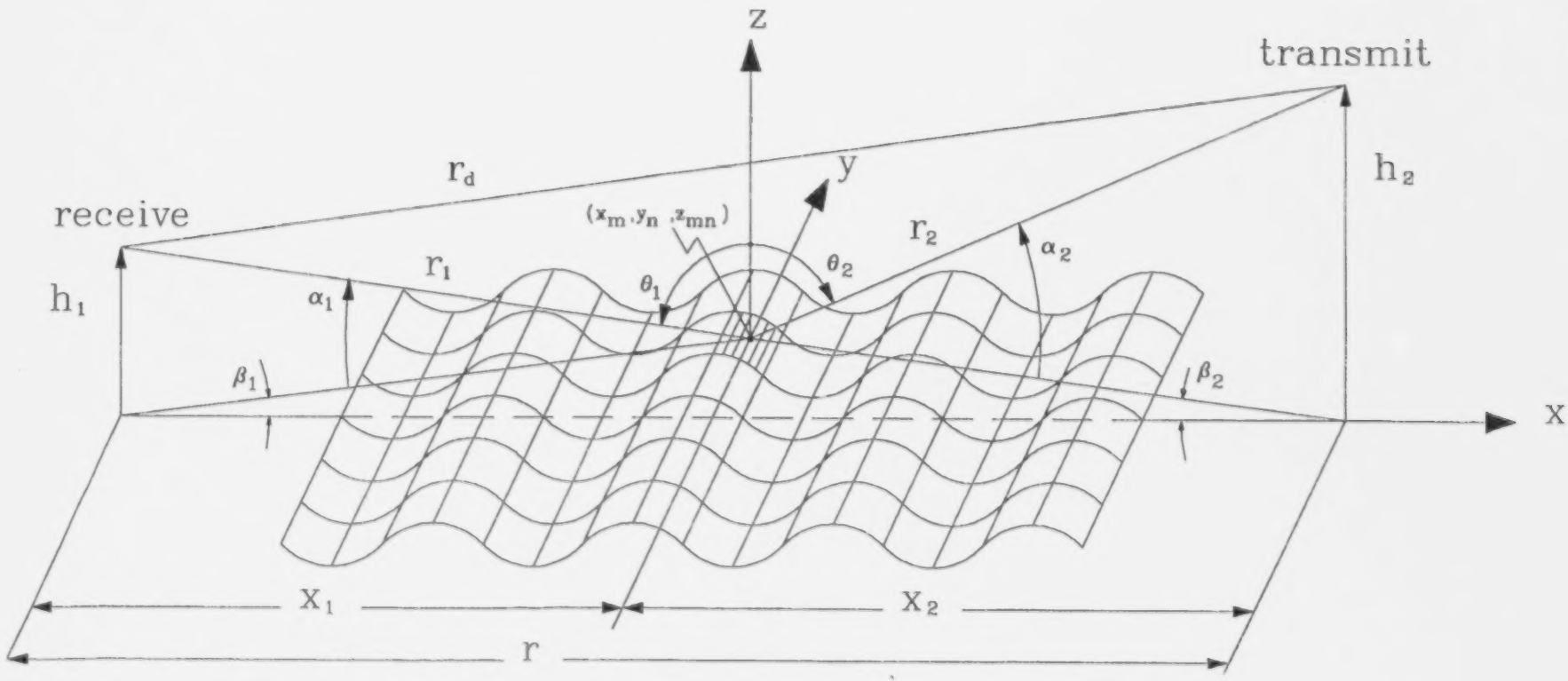

Figure 2: Geometry of the mn'th reflecting facet.

P148367.PDF [Page: 43 of 80]

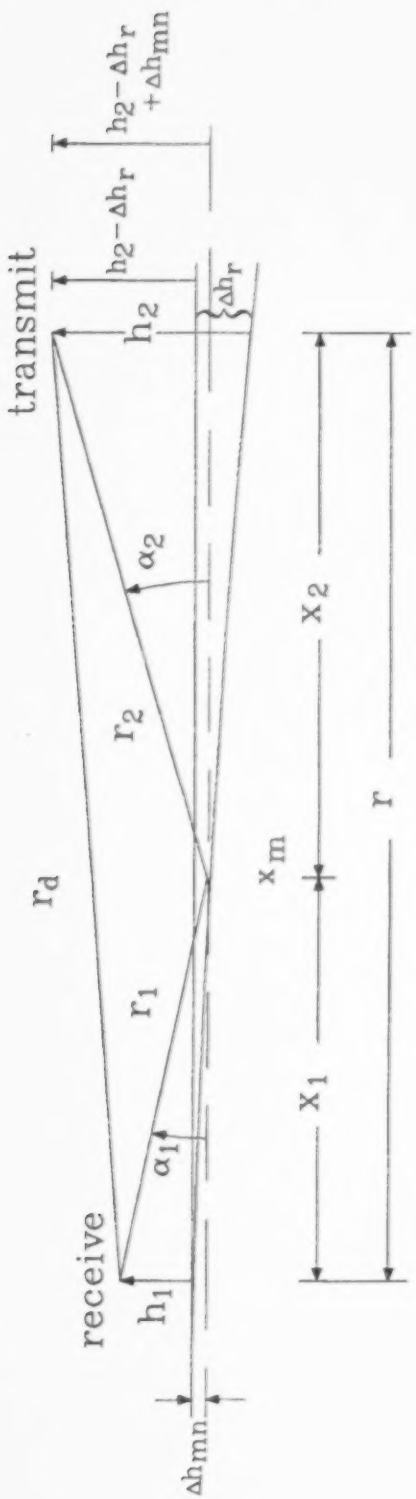

Figure 3: Curved earth geometry.

P148367.PDF [Page: 44 of 80]

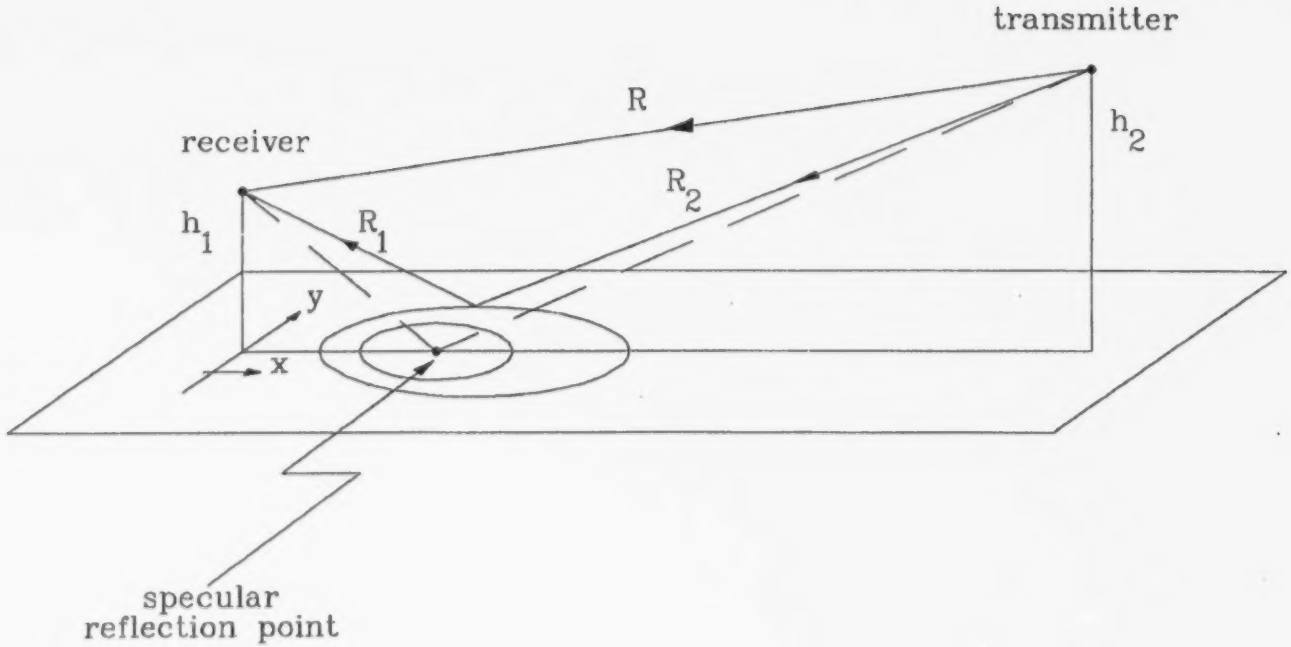

Figure 4: Fresnel zone scattering (after Beckmann and Spizichino)

P148367.PDF [Page: 45 of 80]

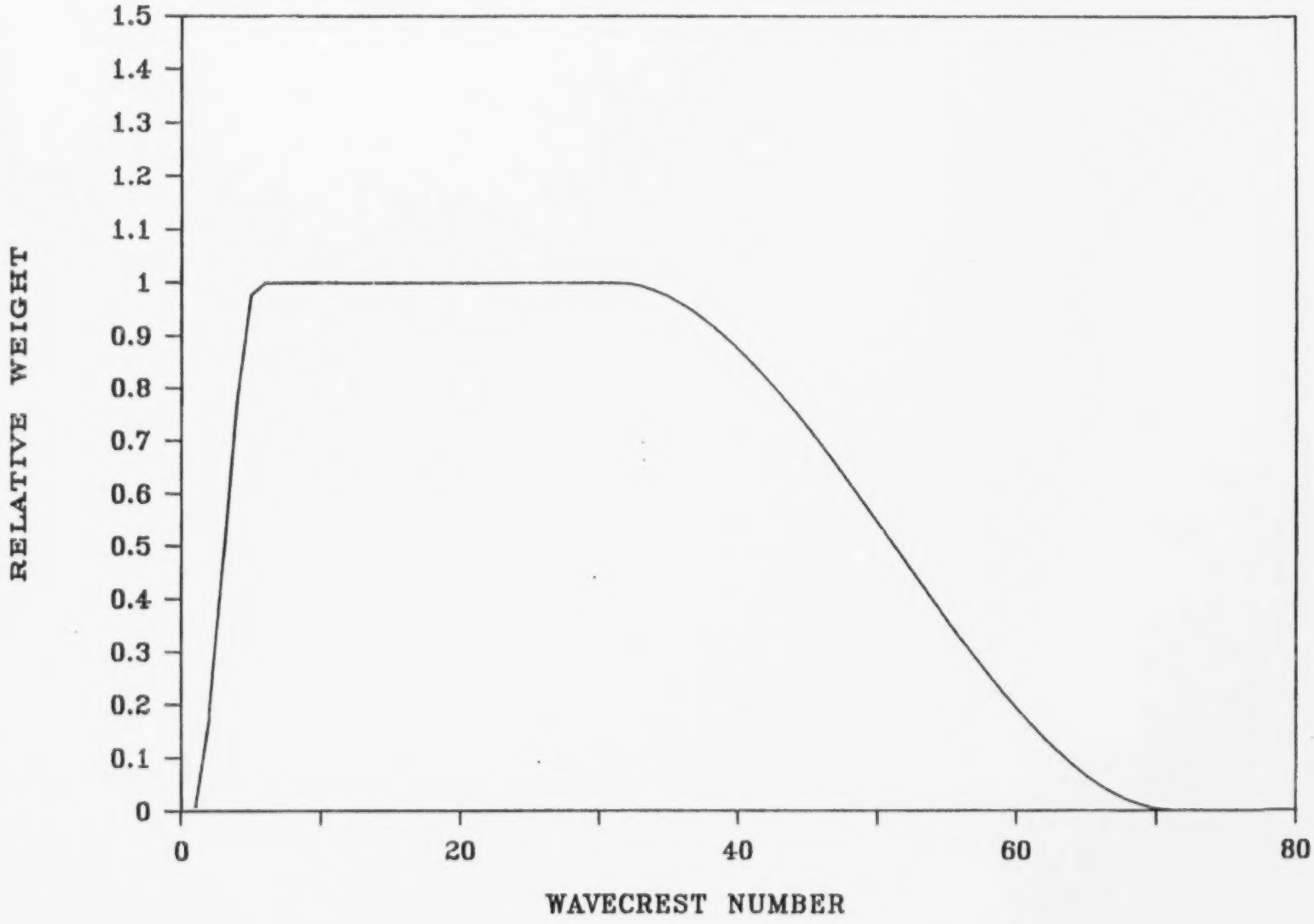

Figure 5: Sample range weighting function for h_1=60', h_2=1060', R=20 nmi (after White and Gery).

(1) Radar Side

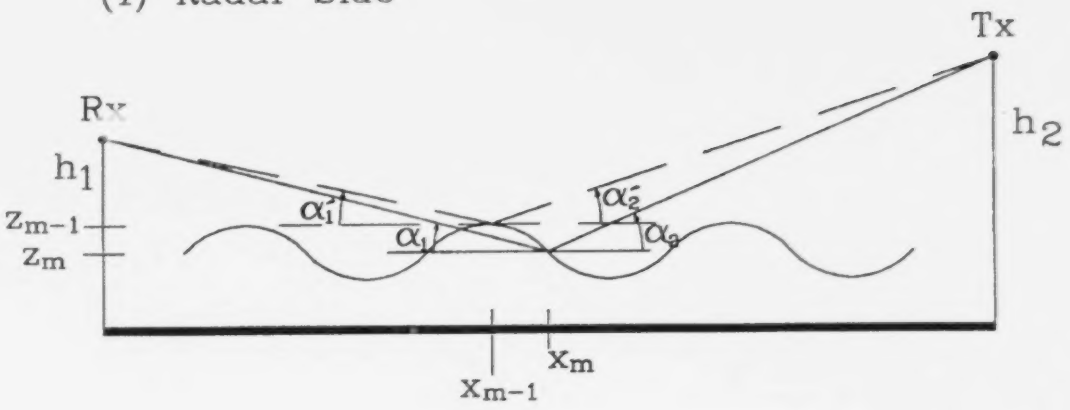

(2) Transmitter Side

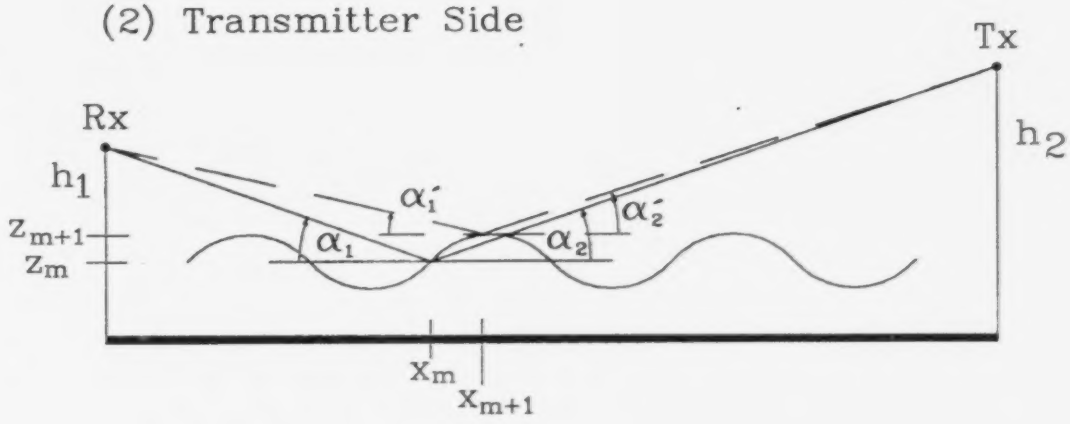

Shadowing occurs in both cases iff:

$$\alpha_1 > \alpha_1'$$

and

$$\alpha_2 > \alpha_2'$$

Figure 6: The shadowing problem illustrated – shadowing on transmitter and radar sides.

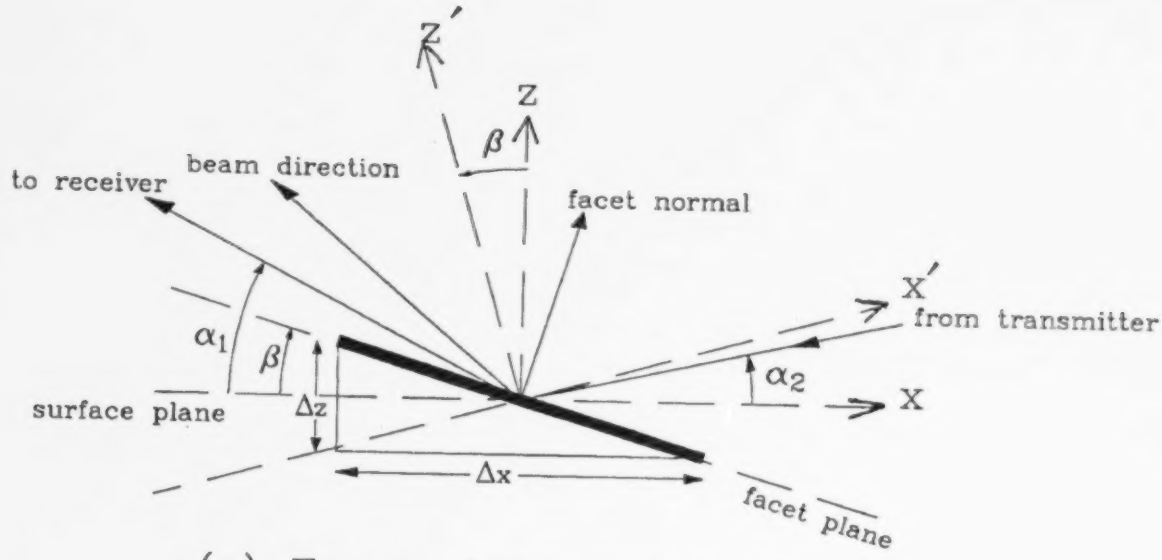

(a) Facet slope wrt x axis
(rotate CCW about y axis)

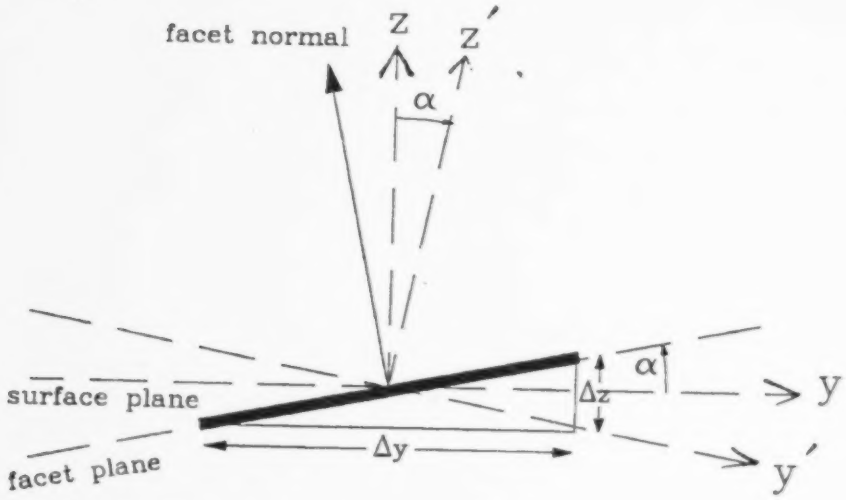

(b) Facet slope wrt y axis
(rotate CW about x axis)

Figure 7: Coordinate rotations to align z axis along beam direction: (a) CCW rotation by β wrt y axis to account for x component of facet slope (b) CW rotation by α wrt x axis to account for y component of facet slope.

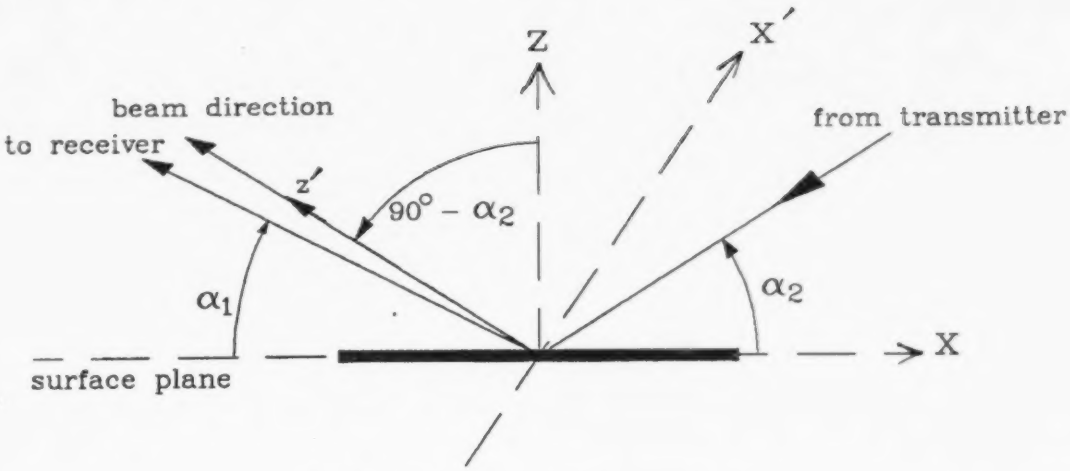

(a) Facet elevation
(rotate CCW about y axis)

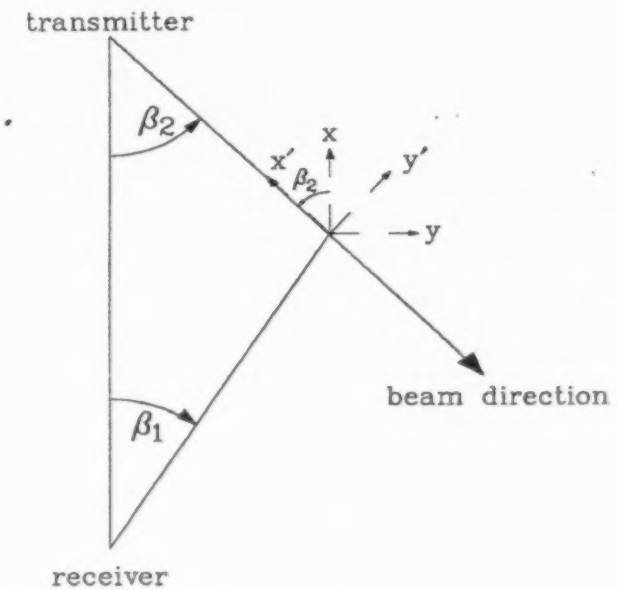

(b) Facet azimuth
(rotate CCW about z axis)

Figure 8: Coordinate rotations to align z axis along beam direction: (a) CCW rotation by $(90–\alpha_2)$ wrt y axis to account for facet elevation (b) CCW rotationn by β_2 wrt z axis to account for facet azimuth.

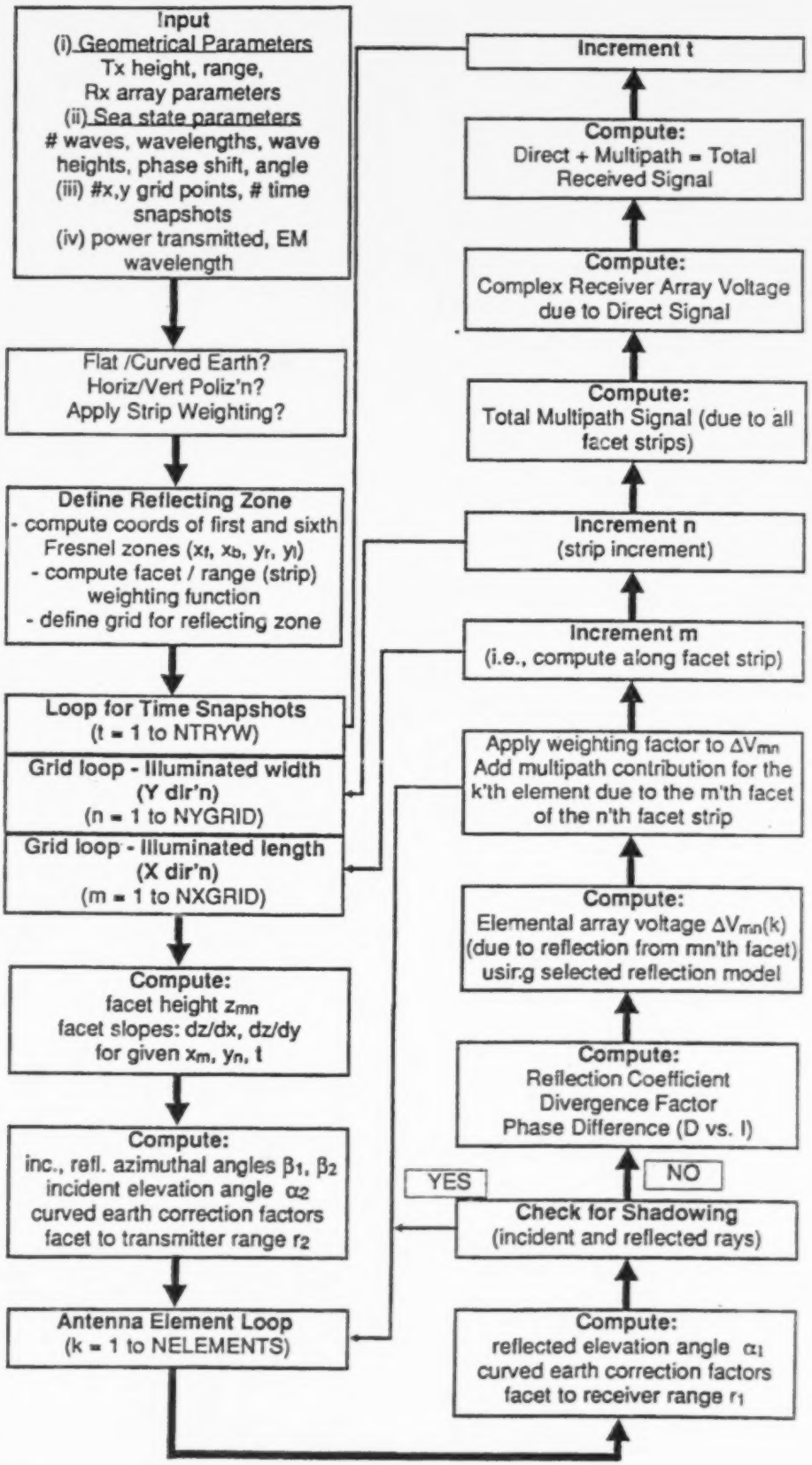
Input
(i) Geometrical Parameters
Tx height, range,
Rx array parameters
(ii) Sea state parameters
waves, wavelengths, wave heights, phase shift, angle
(iii) #x,y grid points, # time snapshots
(iv) power transmitted, EM wavelength
Flat /Curved Earth?
Horiz/Vert Poliz'n?
Apply Strip Weighting?
Define Reflecting Zone
- compute coords of first and sixth Fresnel zones (x_f, x_b, y_r, y_l)
- compute facet / range (strip) weighting function
- define grid for reflecting zone
Loop for Time Snapshots
(t = 1 to NTRYW)
Grid loop - Illuminated width
(Y dir'n)
(n = 1 to NYGRID)
Grid loop - Illuminated length
(X dir'n)
(m = 1 to NXGRID)
Compute:
facet height z_{mn}
facet slopes: dz/dx, dz/dy
for given x_m, y_n, t
Compute:
inc., refl. azimuthal angles β_1, β_2
incident elevation angle α_2
curved earth correction factors
facet to transmitter range r_2
Antenna Element Loop
(k = 1 to NELEMENTS)
Compute:
reflected elevation angle α_1
curved earth correction factors
facet to receiver range r_1
Check for Shadowing
(incident and reflected rays)
YES
NO
Compute:
Reflection Coefficient
Divergence Factor
Phase Difference (D vs. I)
Compute:
Elemental array voltage $\Delta V_{mn}(k)$
(due to reflection from mn'th facet)
using selected reflection model
Apply weighting factor to ΔV_{mn}
Add multipath contribution for the k'th element due to the m'th facet of the n'th facet strip
Increment m
(i.e., compute along facet strip)
Increment n
(strip increment)
Compute:
Total Multipath Signal (due to all facet strips)
Compute:
Complex Receiver Array Voltage due to Direct Signal
Compute:
Direct + Multipath = Total Received Signal
Increment t

Figure 9: Sea swell modeling software block diagram.

P148367.PDF [Page: 50 of 80]

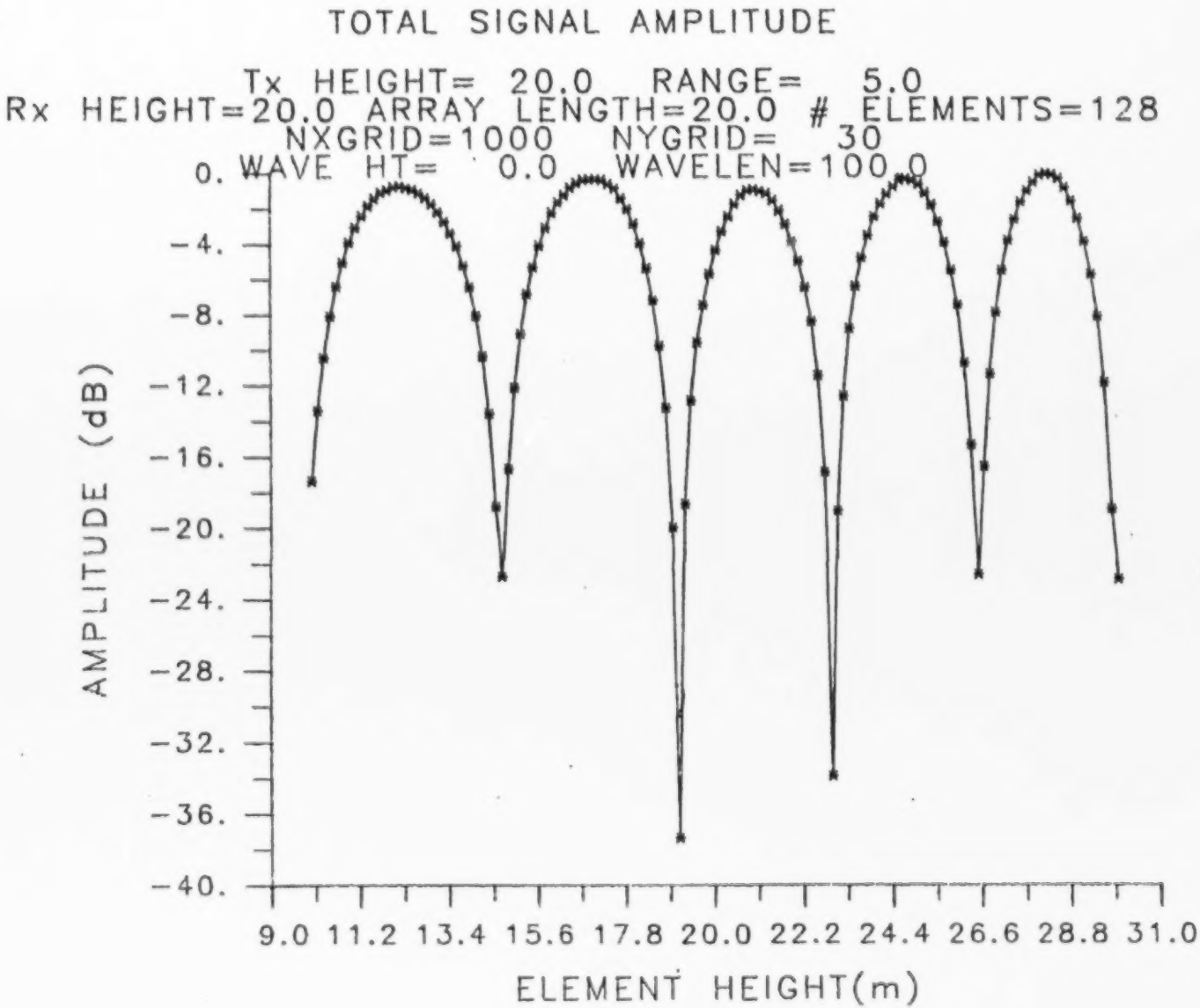

Figure 10(a): Received amplitude: h_1=h2=20 m, range=5 km, zero sea state – path difference with respect to centre of array.

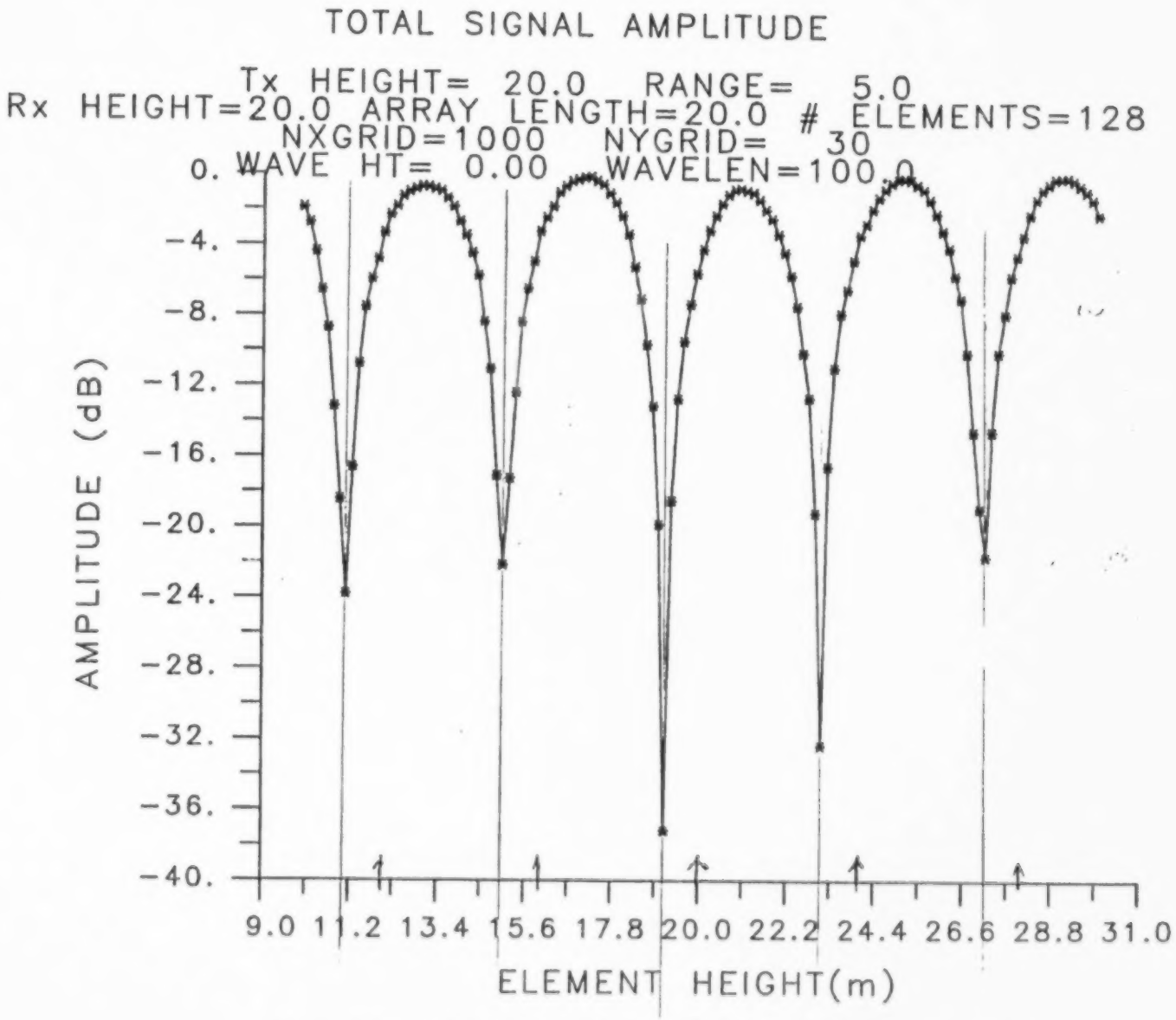

Figure 10(b): Received amplitude: h_1=h2=20 m, range=5 km, zero sea state – path difference with respect to antenna elements.

P148367.PDF [Page: 51 of 80]

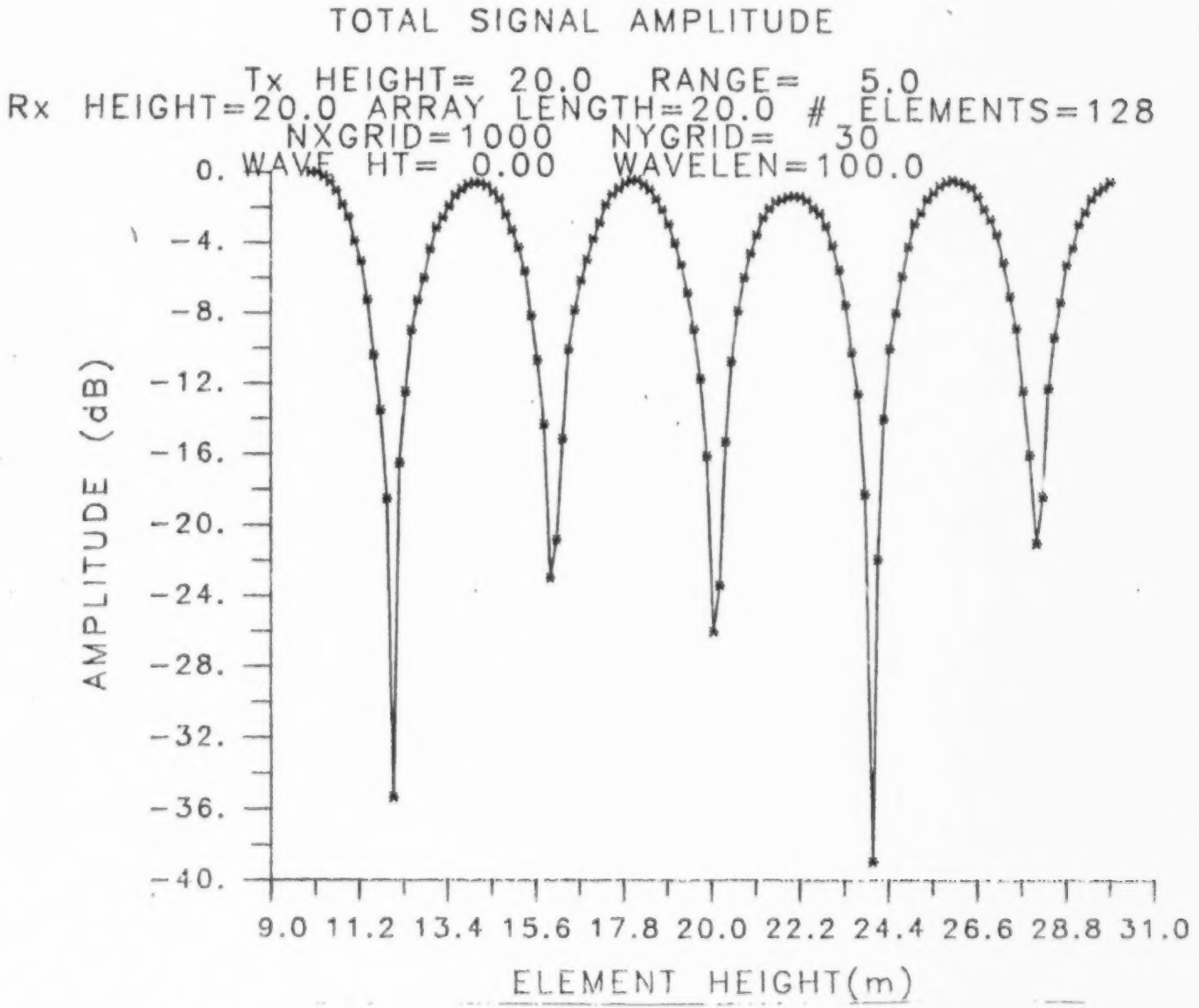

Figure 11(a): Received amplitude: flat earth model, same parameters as

P148367.PDF [Page: 52 of 80]

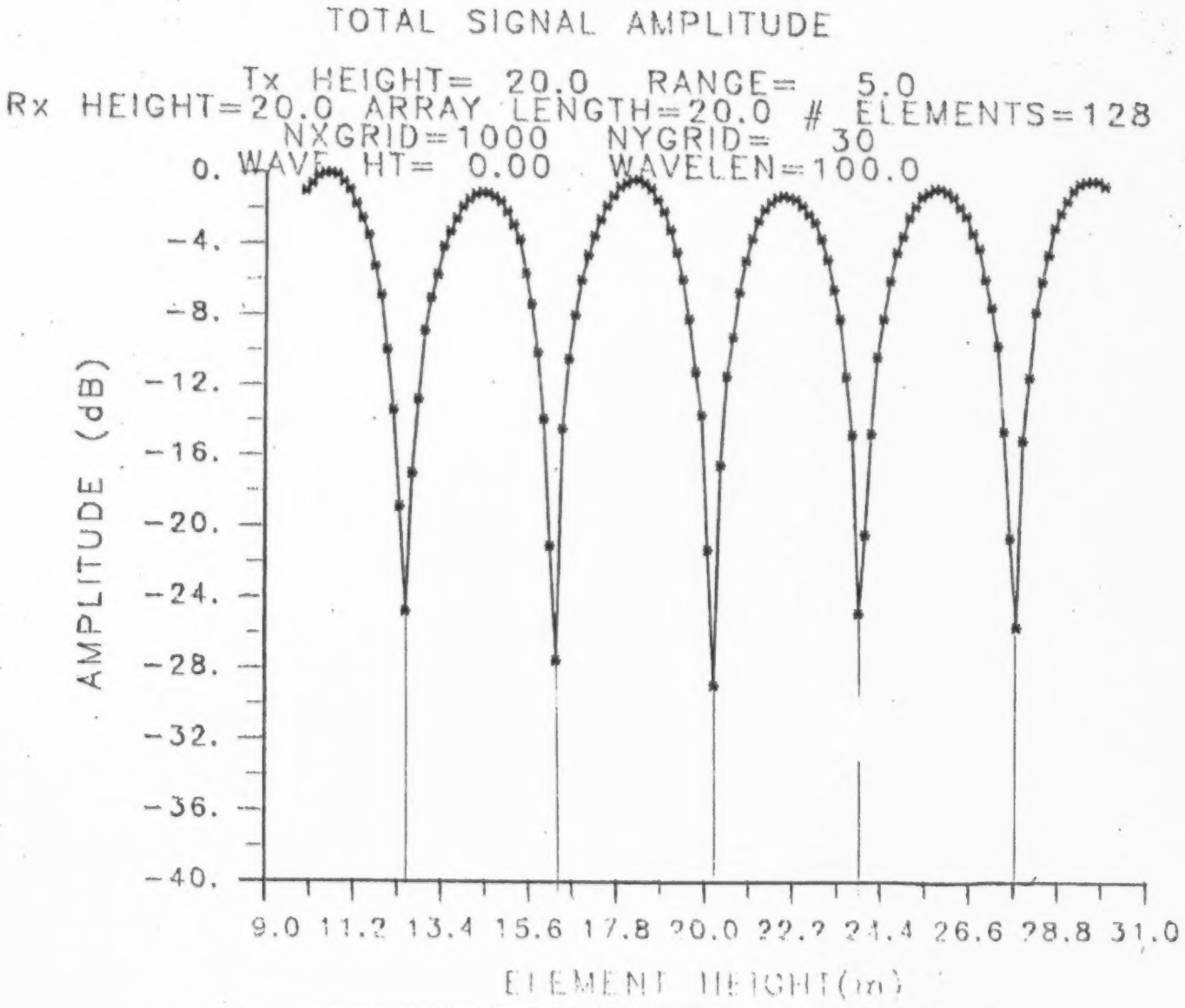

Figure 11(b): Received amplitude: curved earth model, same parameters as Figure 10 except 90° phase correction included.

P148367.PDF [Page: 53 of 80]

P148367.PDF [Page: 54 of 80]

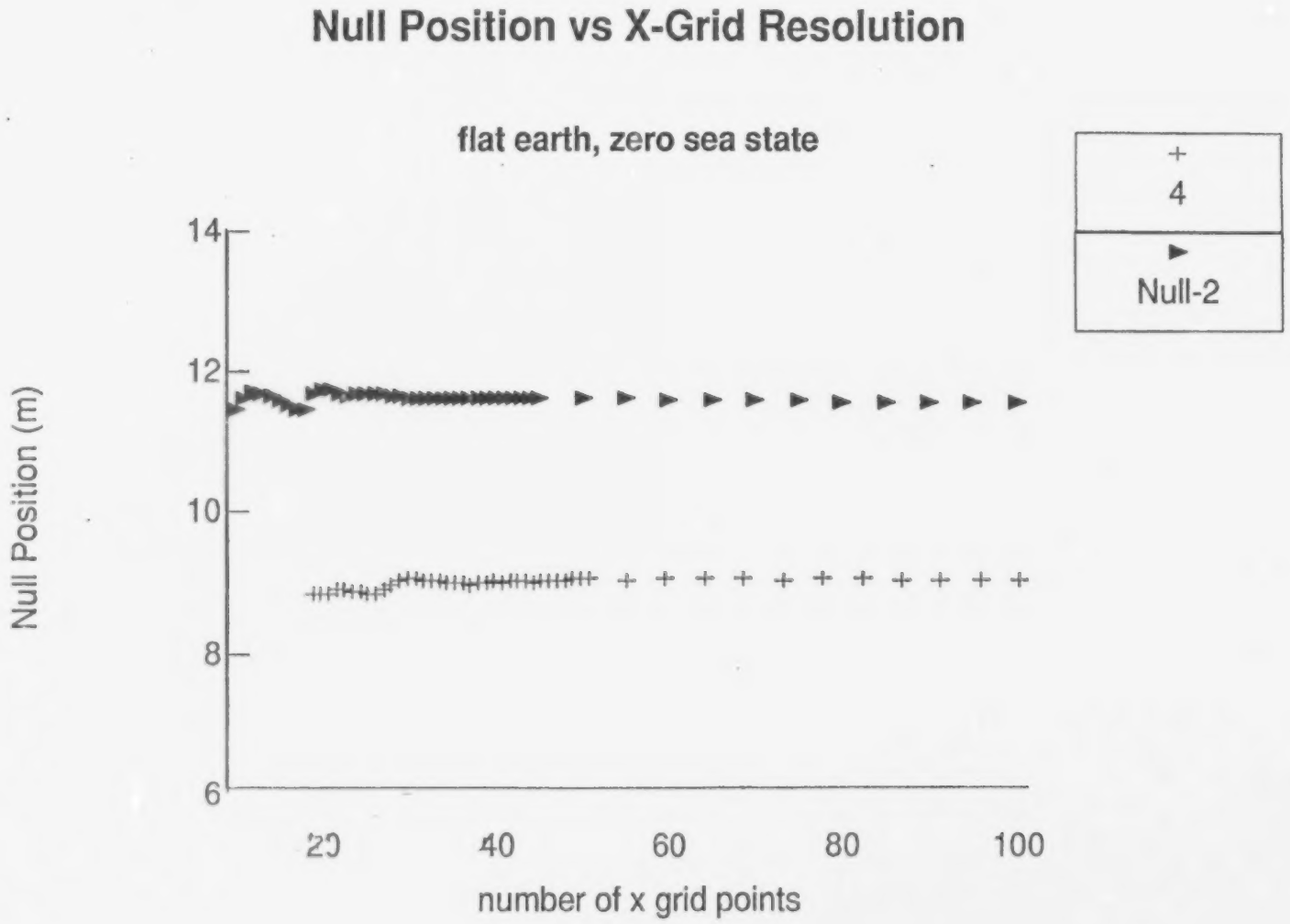

Figure 12(a): Null positions versus varying range grid resolution (h_1=10

P148367.PDF [Page: 55 of 80]

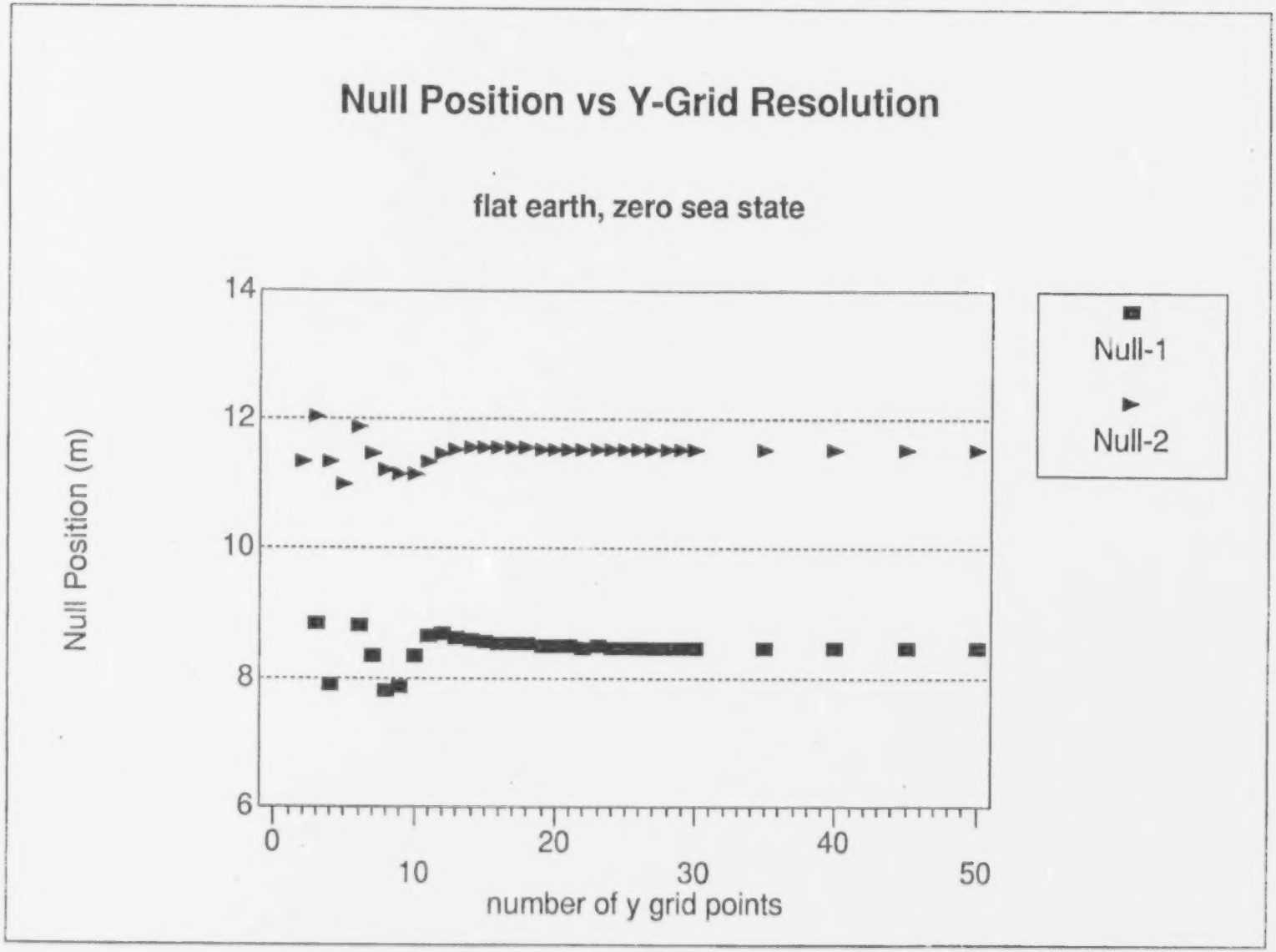

Figure 12(b): Null positions versus varying width grid resolution (h_1=10 m. h_2=20 m. range=2 km).

P148367.PDF [Page: 56 of 80]

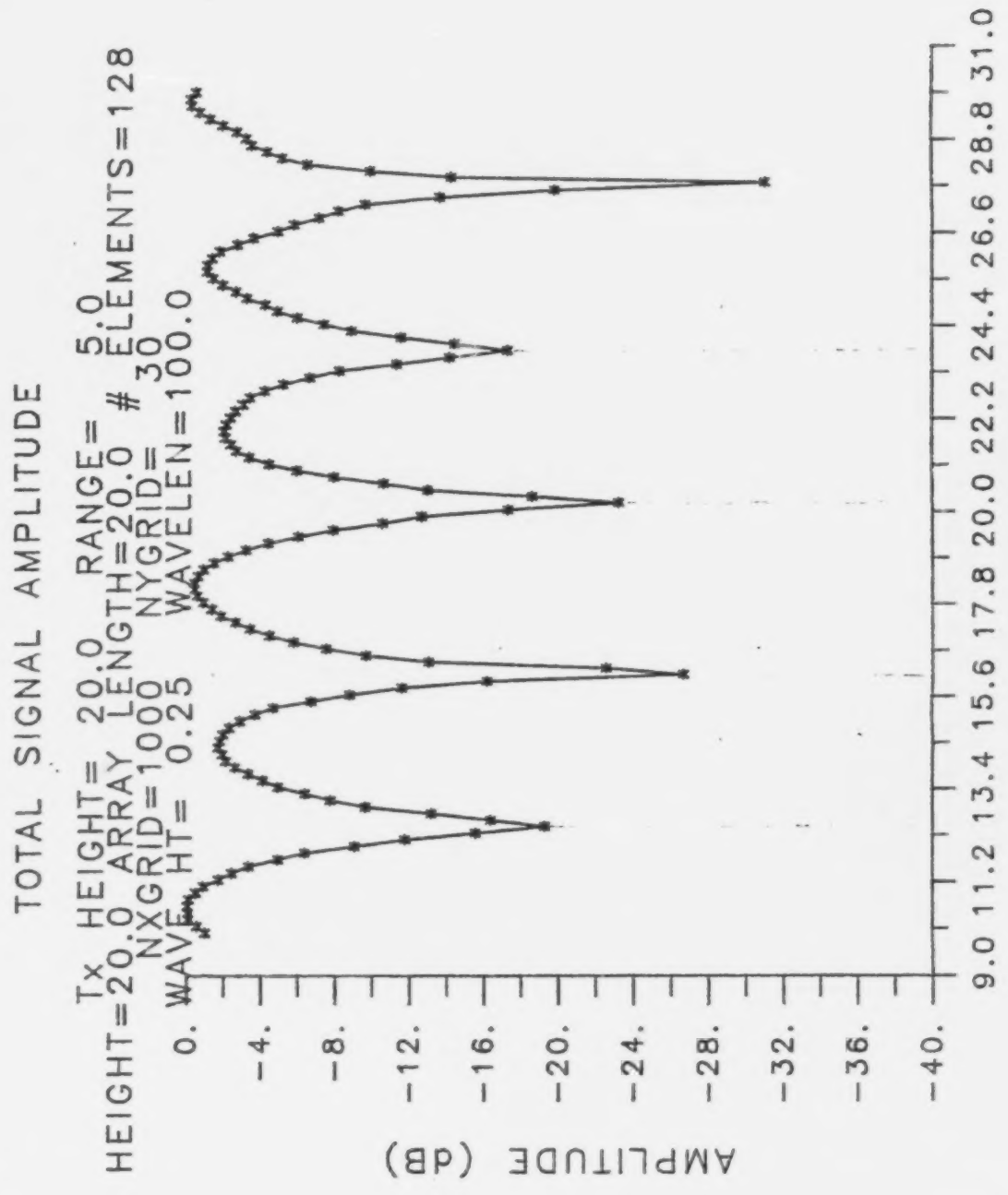

Figure 13(a): Received amplitude: same parameters as in Figure 11(a) except wave height = 0.25 m (peak-to-peak)

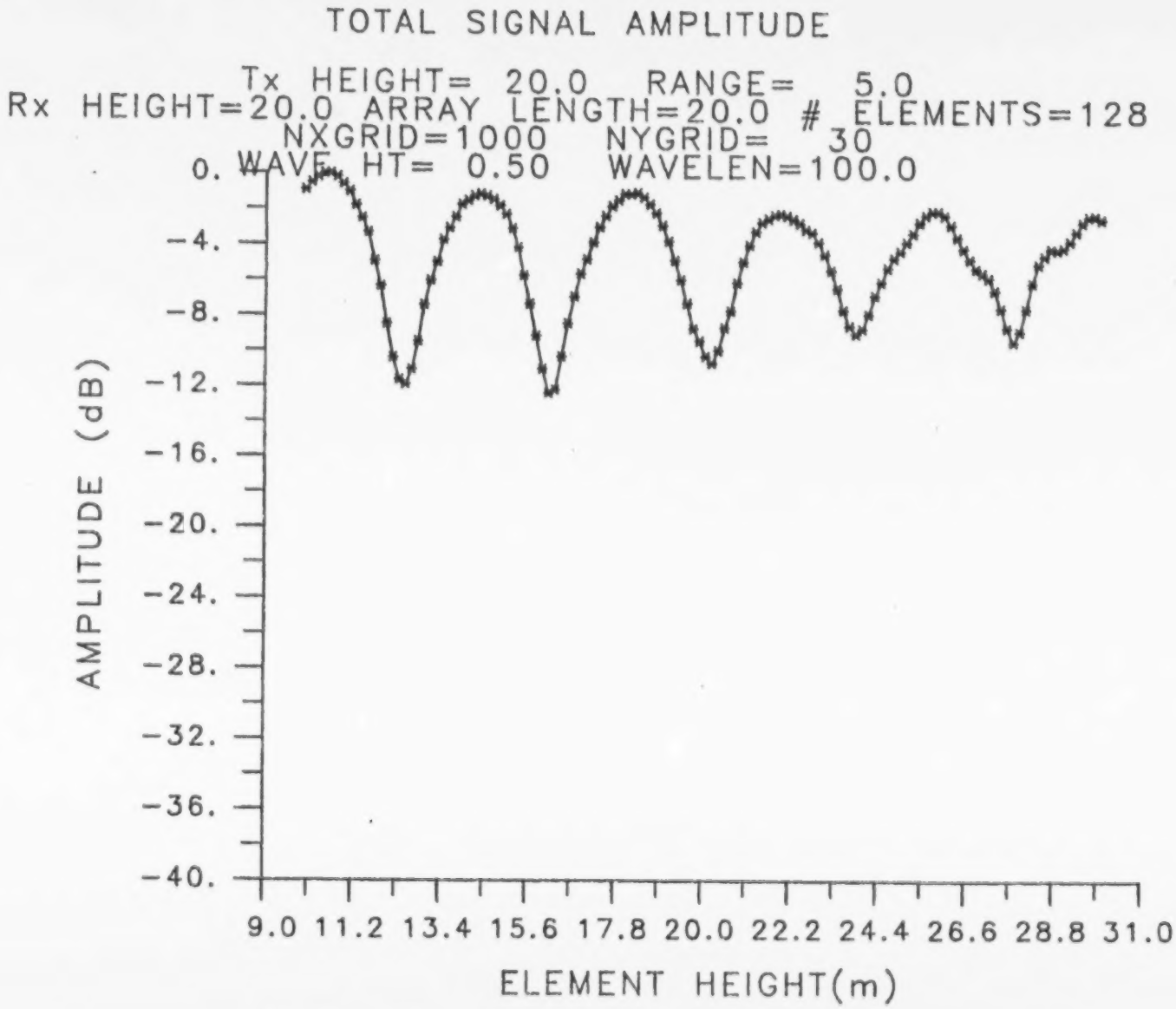

Figure 13(b): Received amplitude: same parameters as in Figure 11(a) except wave height = 0.50 m (peak–to–peak).

P148367.PDF [Page: 57 of 80]

P148367.PDF [Page: 58 of 80]

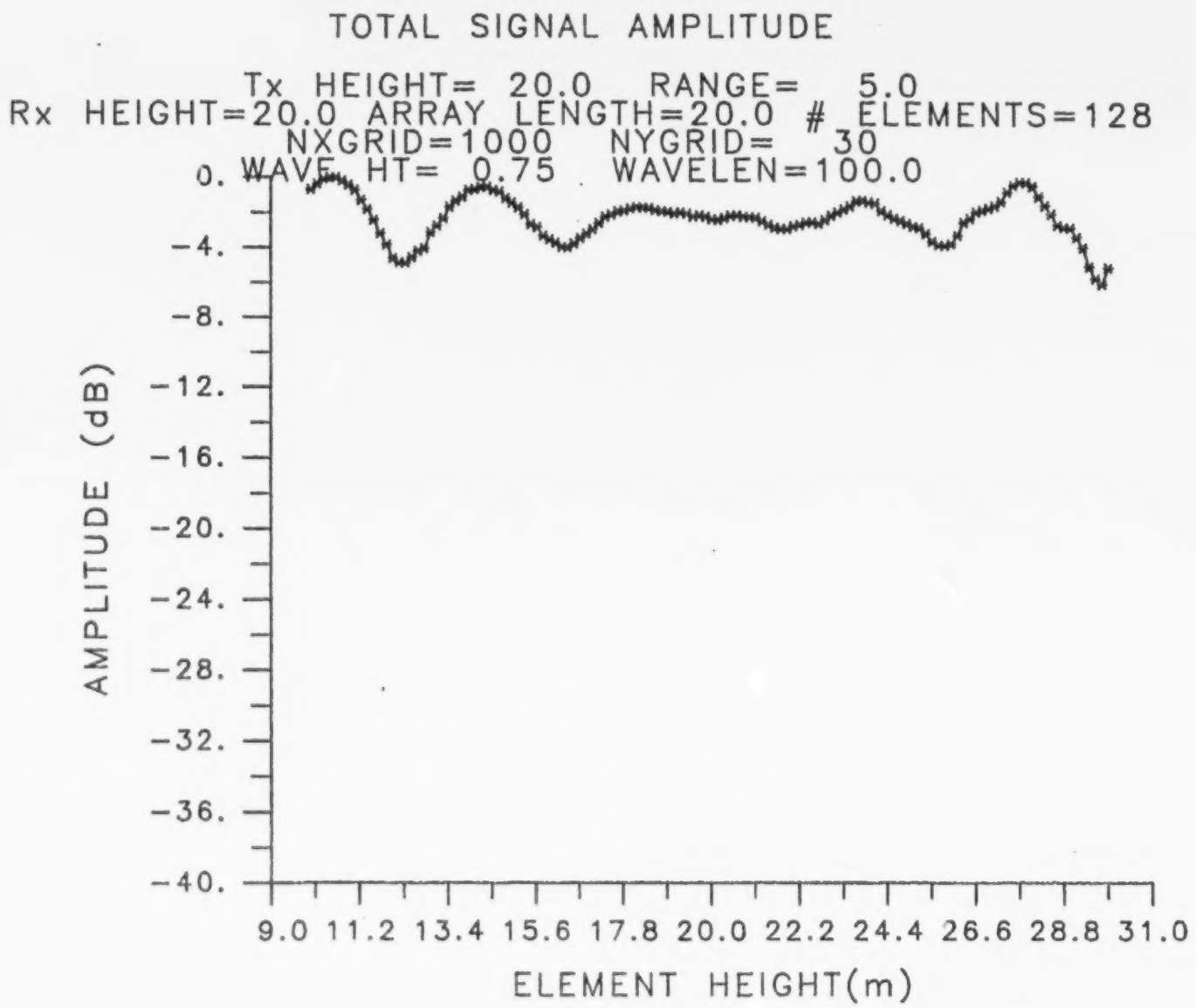

Figure 13(c): Received amplitude: same parameters as in Figure 11(a) except wave height = 0.75 m (peak-to-peak).

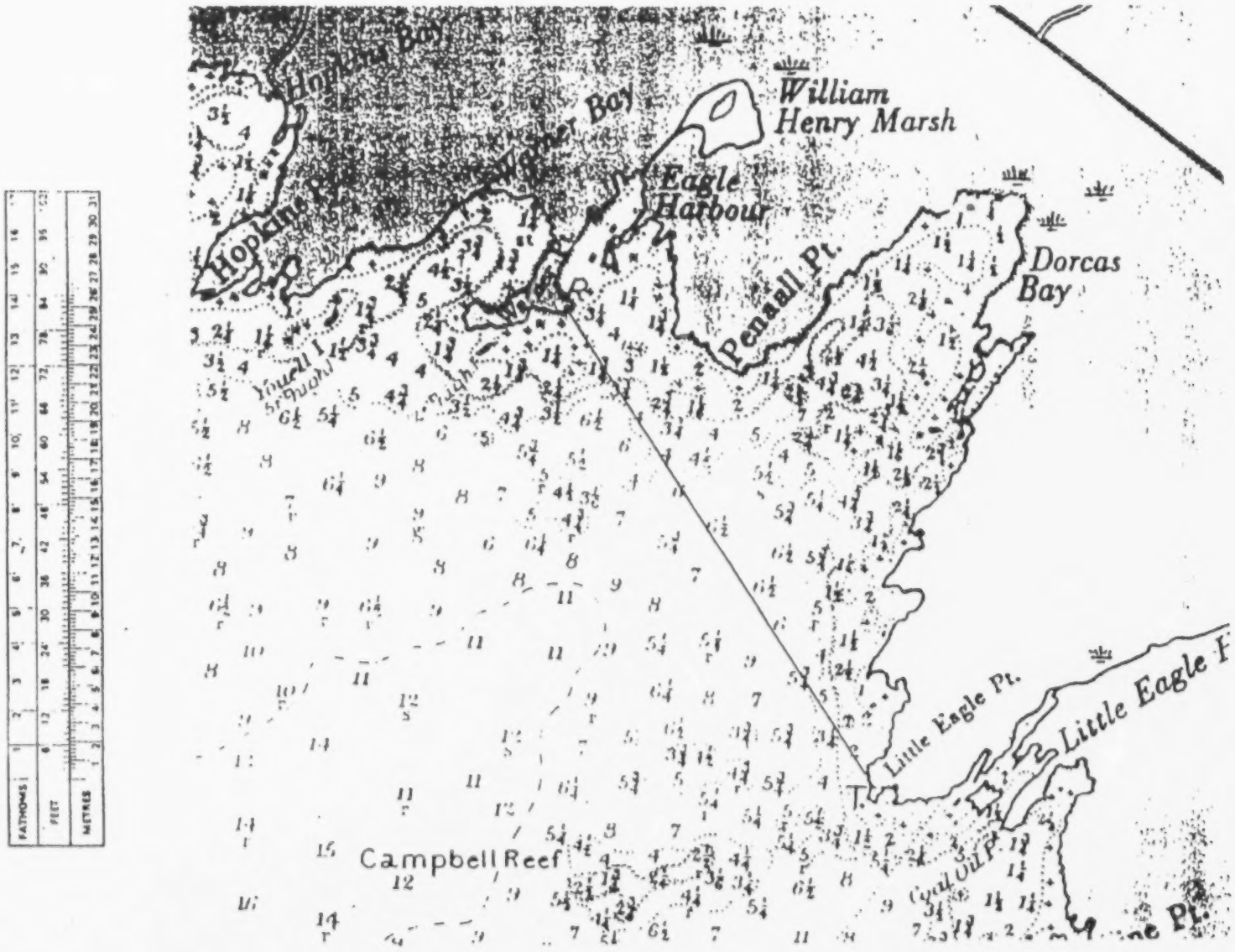

Figure 14: Geography of the Lake Huron Measurement site.

P148367.PDF [Page: 59 of 80]

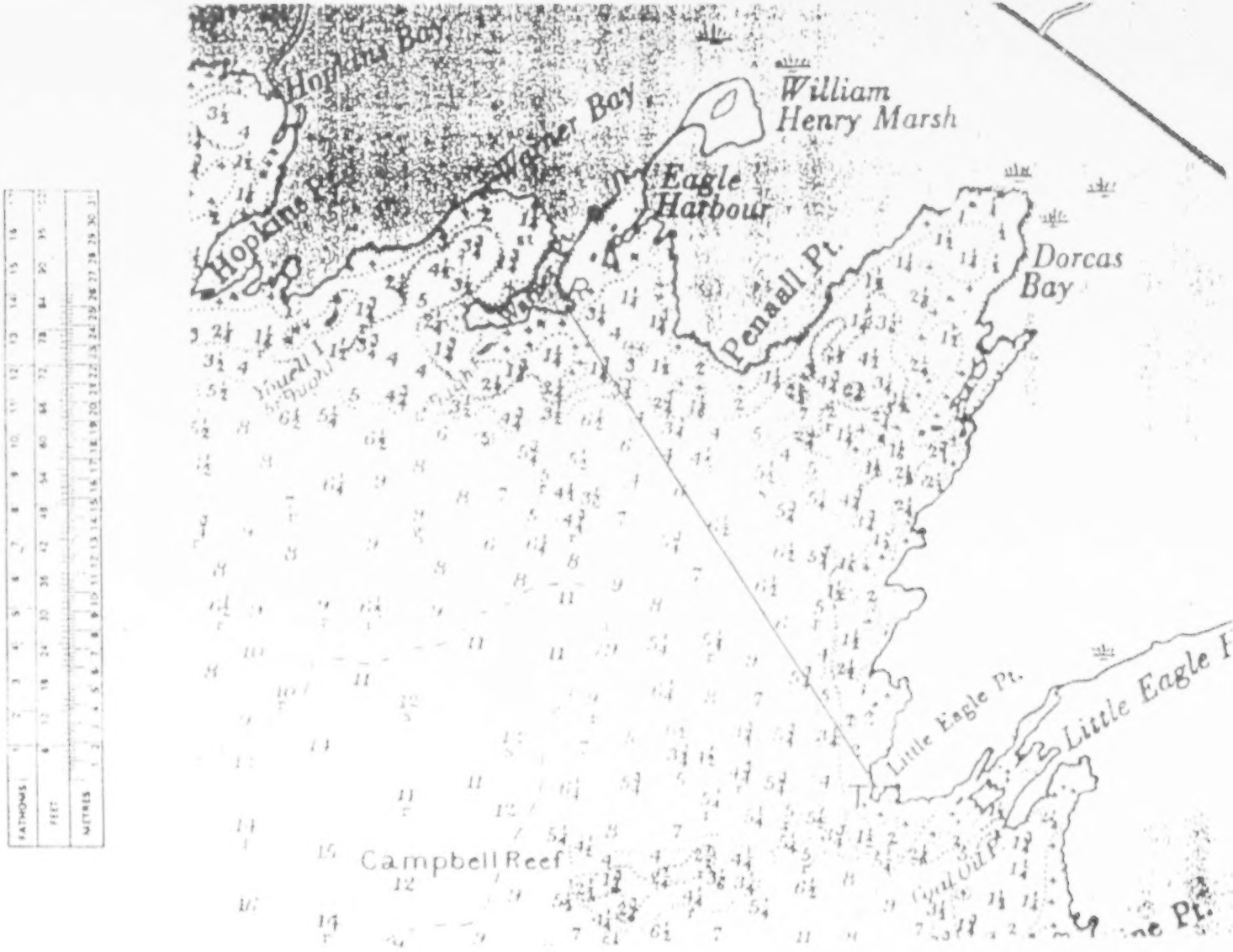

Figure 14: Geography of the Lake Huron Measurement site.

P148367.PDF [Page: 60 of 80]

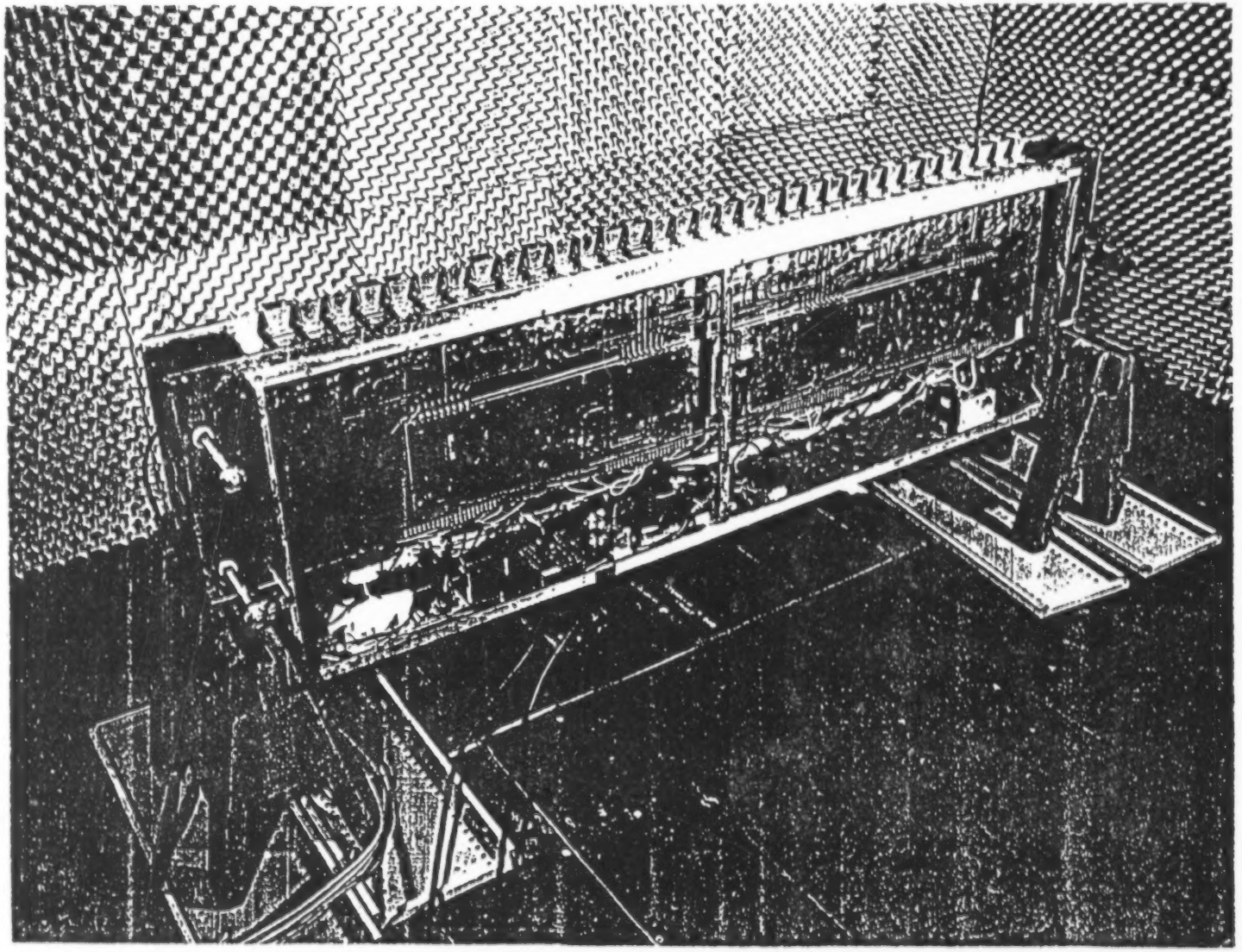

Figure 15: Physical view of the sampled aperture array.

P148367.PDF [Page: 61 of 80]

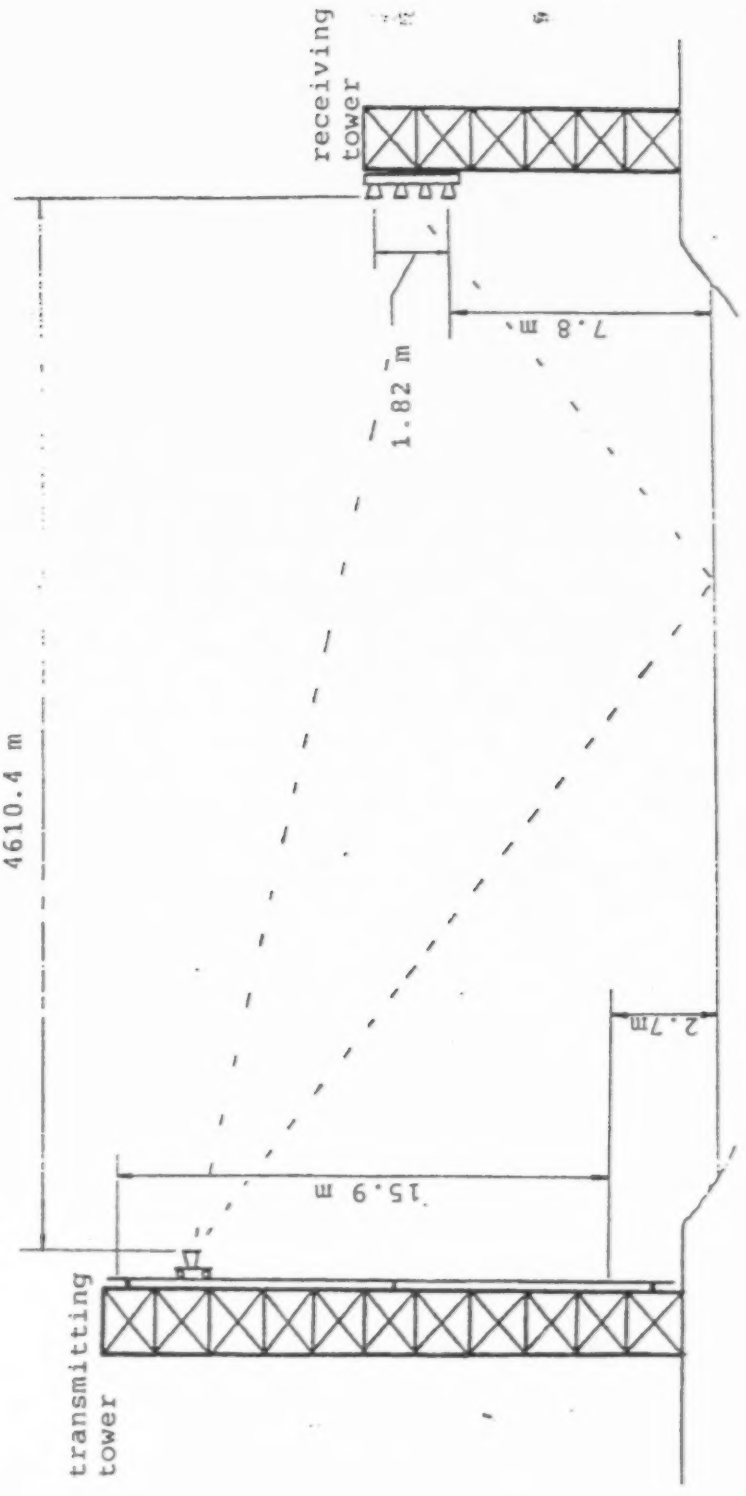

Figure 16: Geometrical parameters of the measurement setup.

P148367.PDF [Page: 62 of 80]

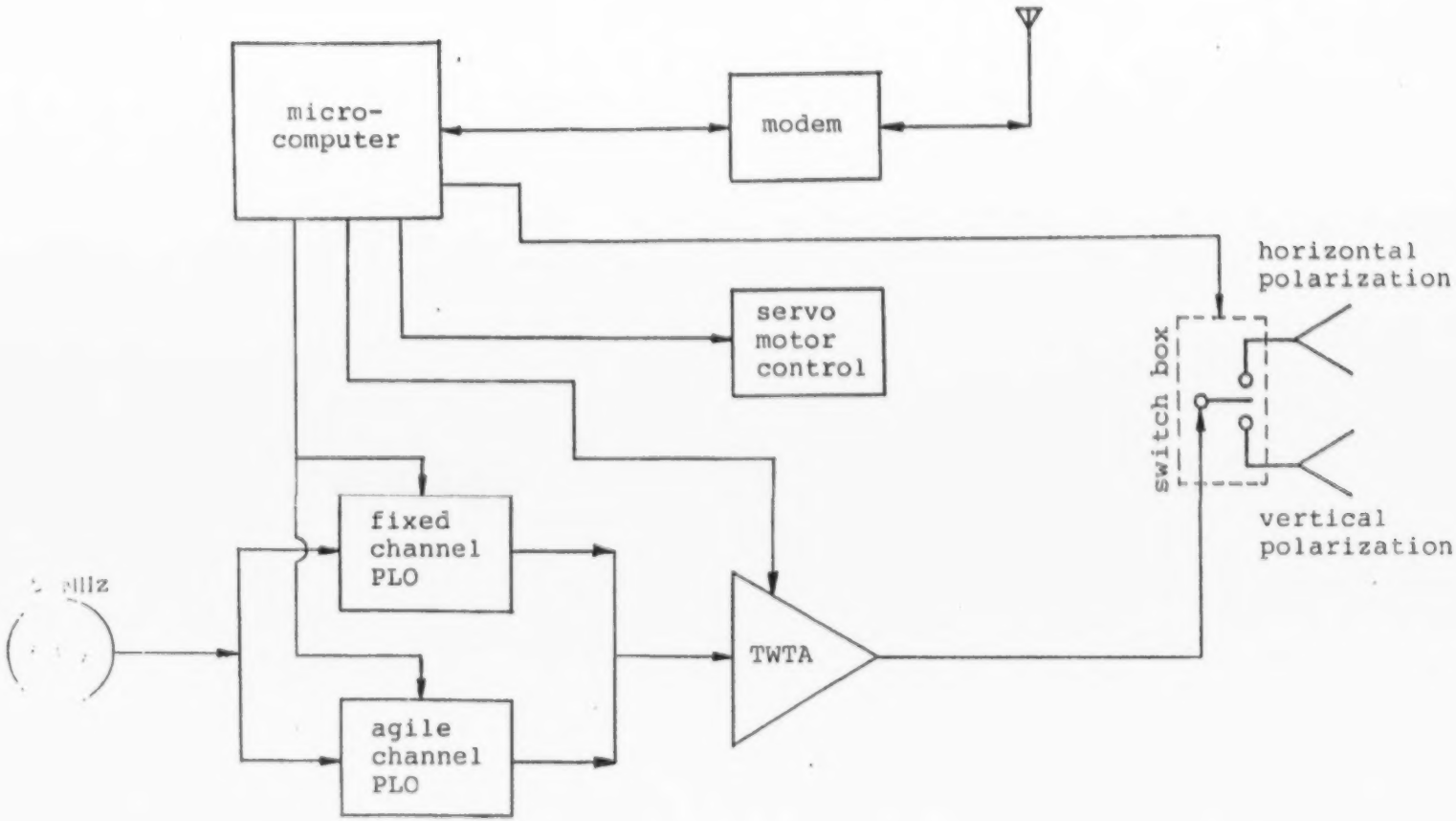

Figure 17: The transmitter system.

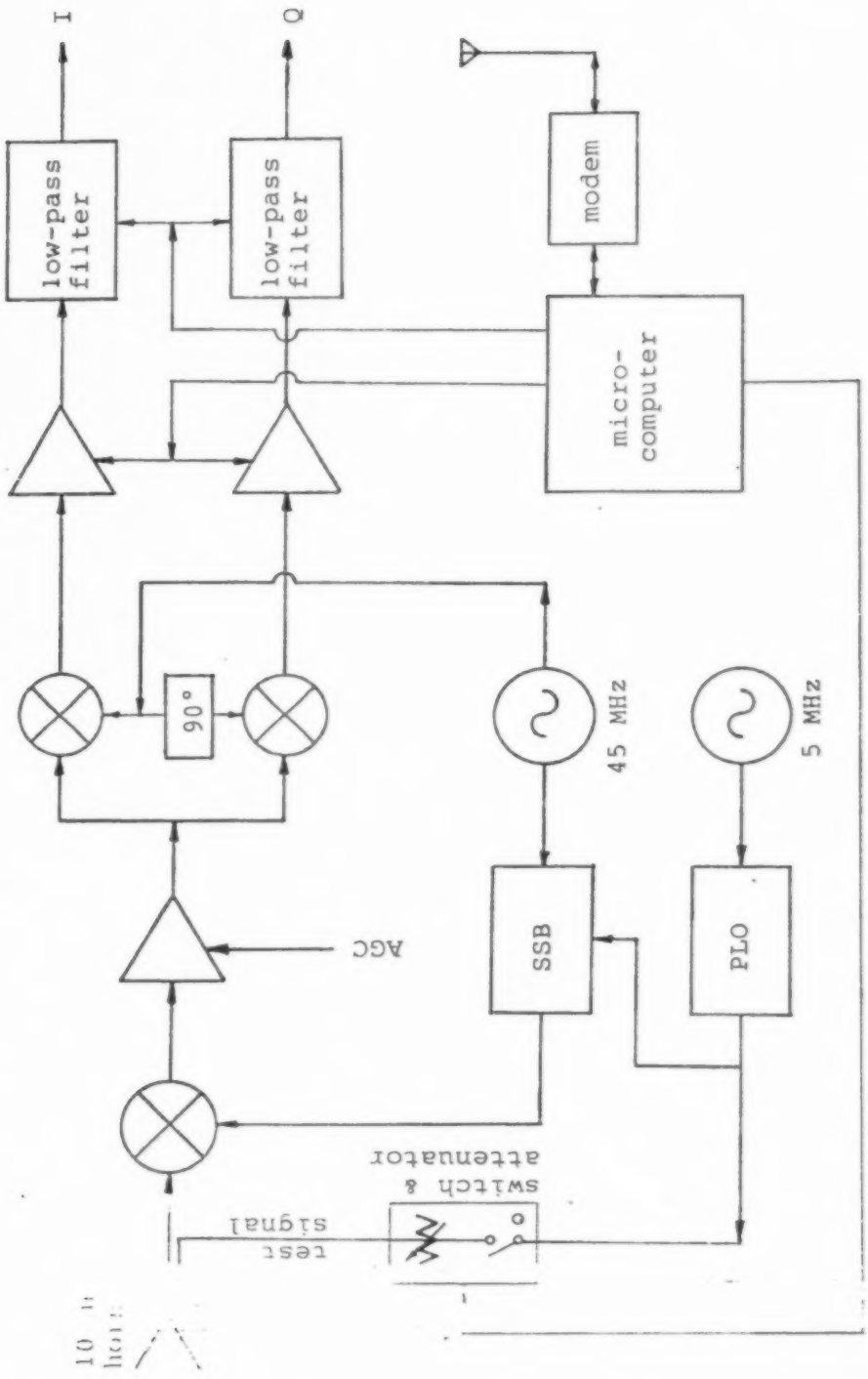

Figure 18: The receiver system.

P148367.PDF [Page: 64 of 80]

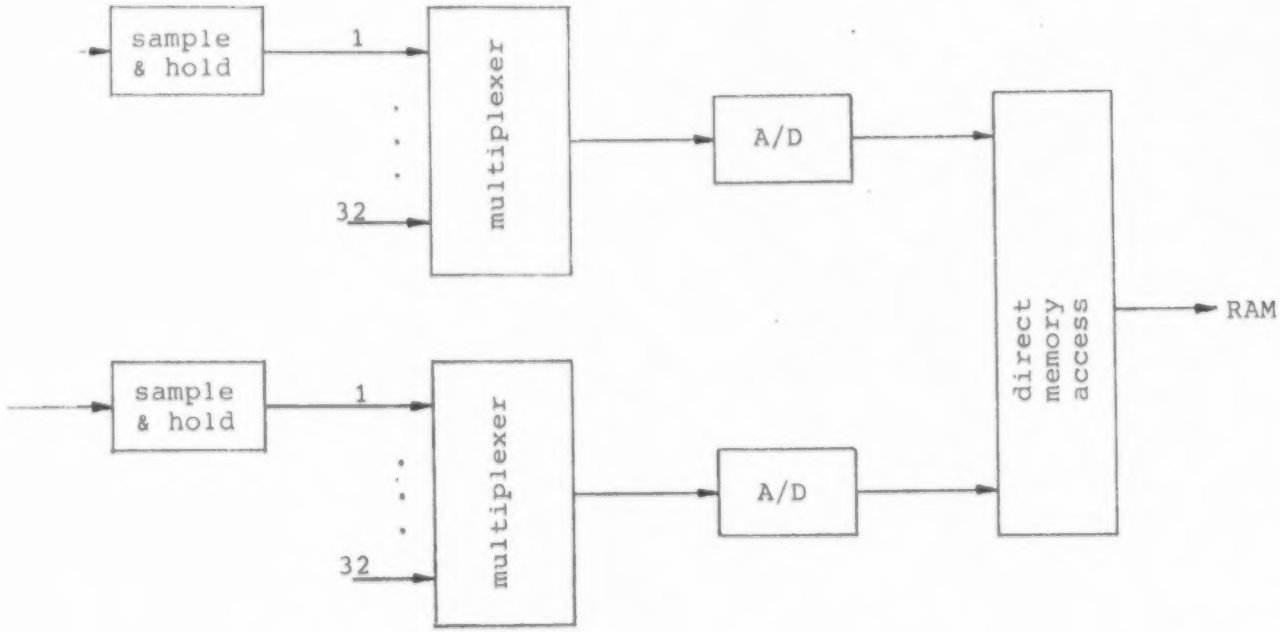

Figure 19: The data acquisition system.

P148367.PDF [Page: 65 of 80]

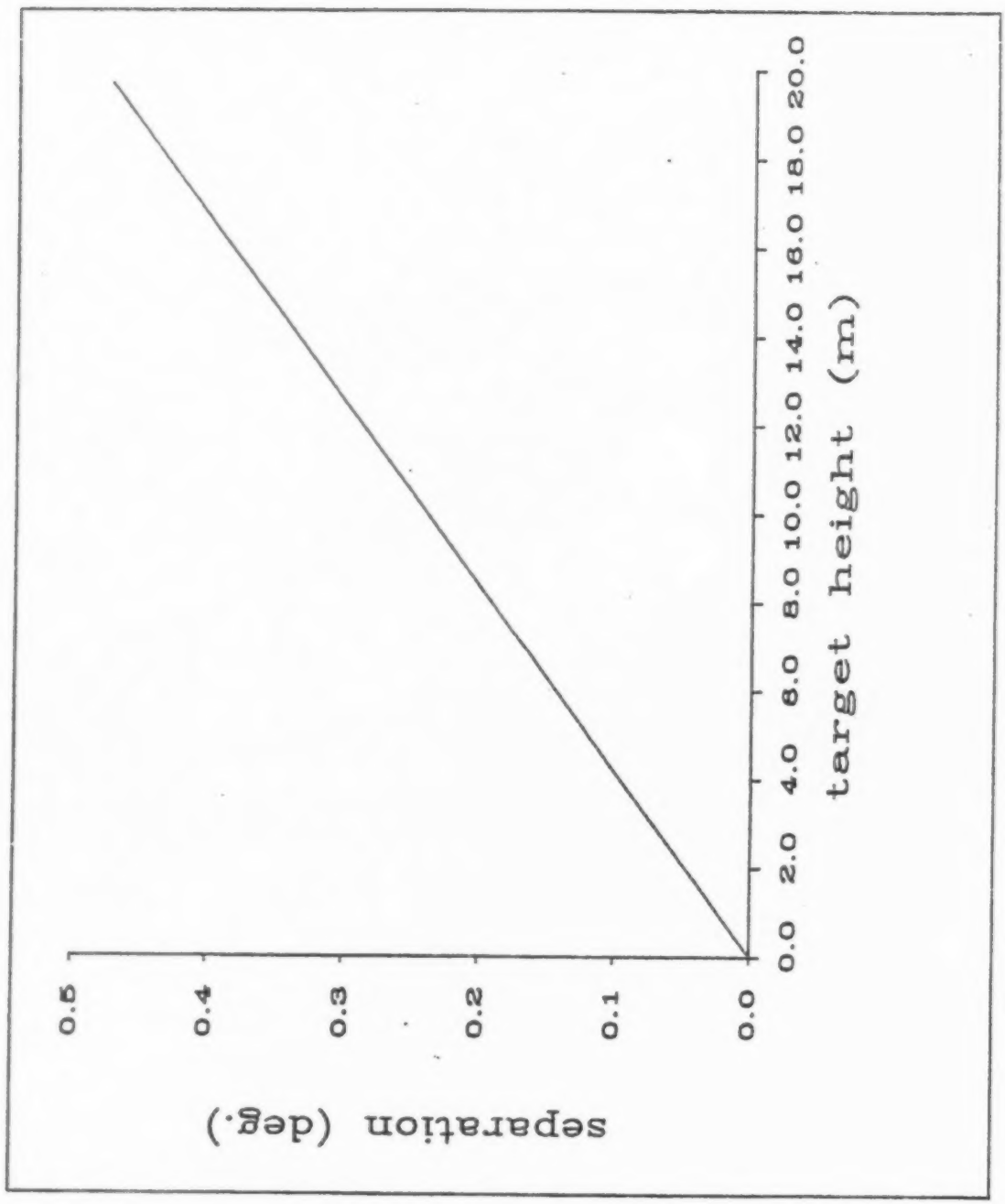

Figure 20: Angular separation of direct and indirect signals versus target height.

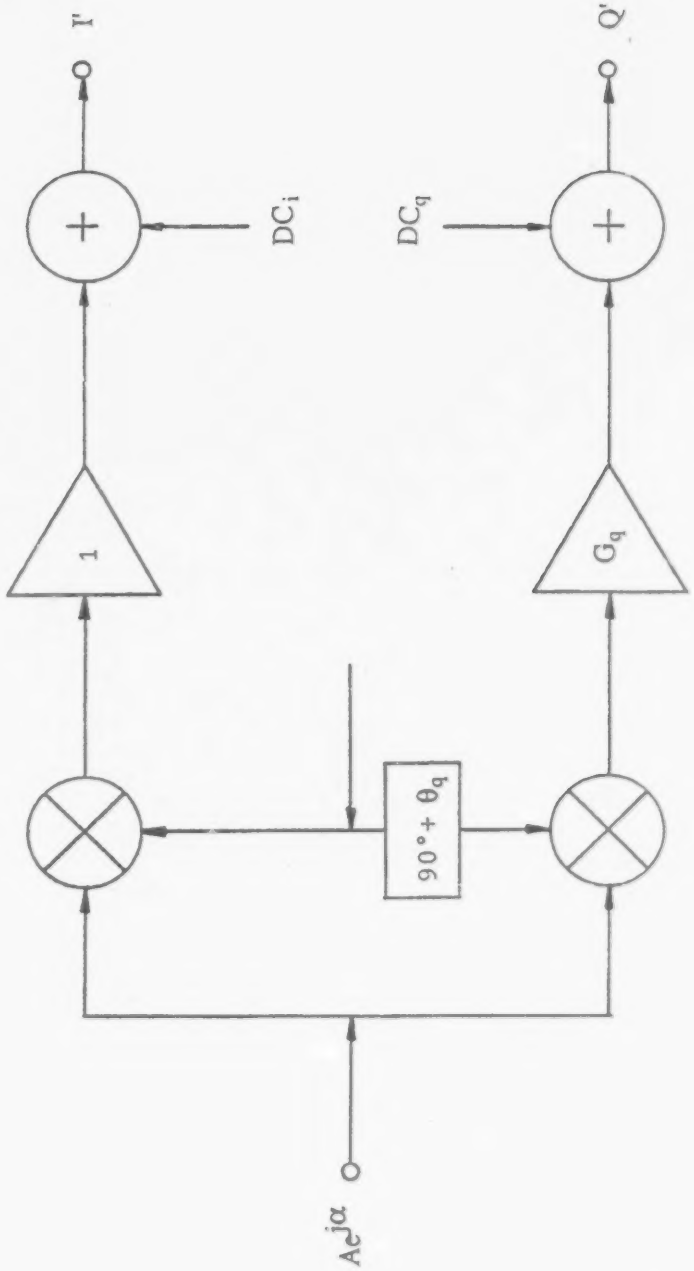

Figure 21: Channel model for IQ calibration.

P148367.PDF [Page: 67 of 80]

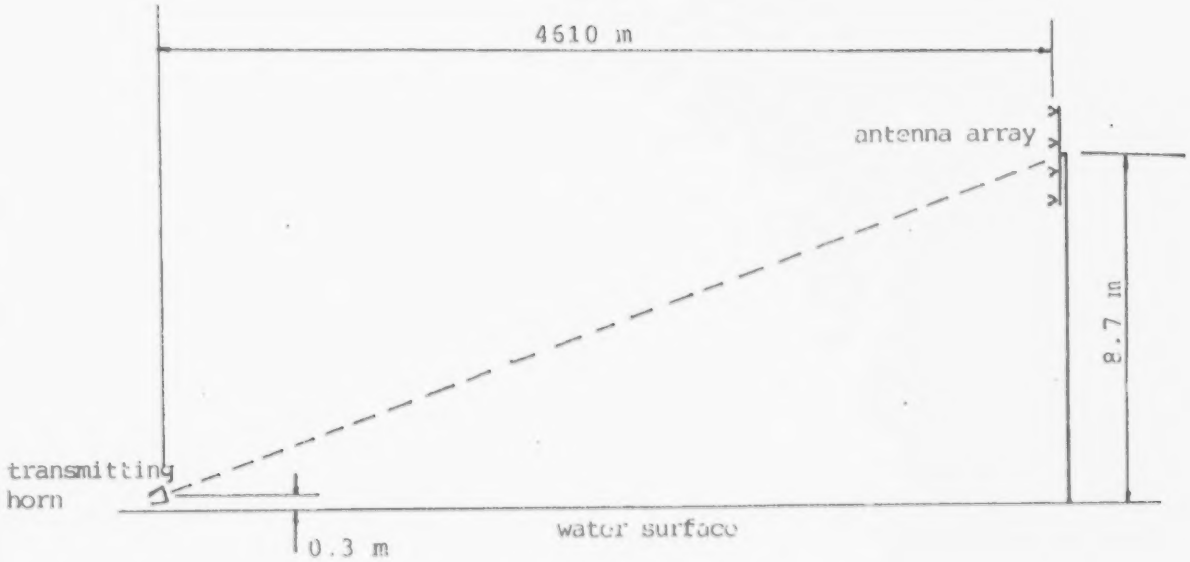

Figure 22: Depiction of far–field calibration procedure.

P148367.PDF [Page: 68 of 80]

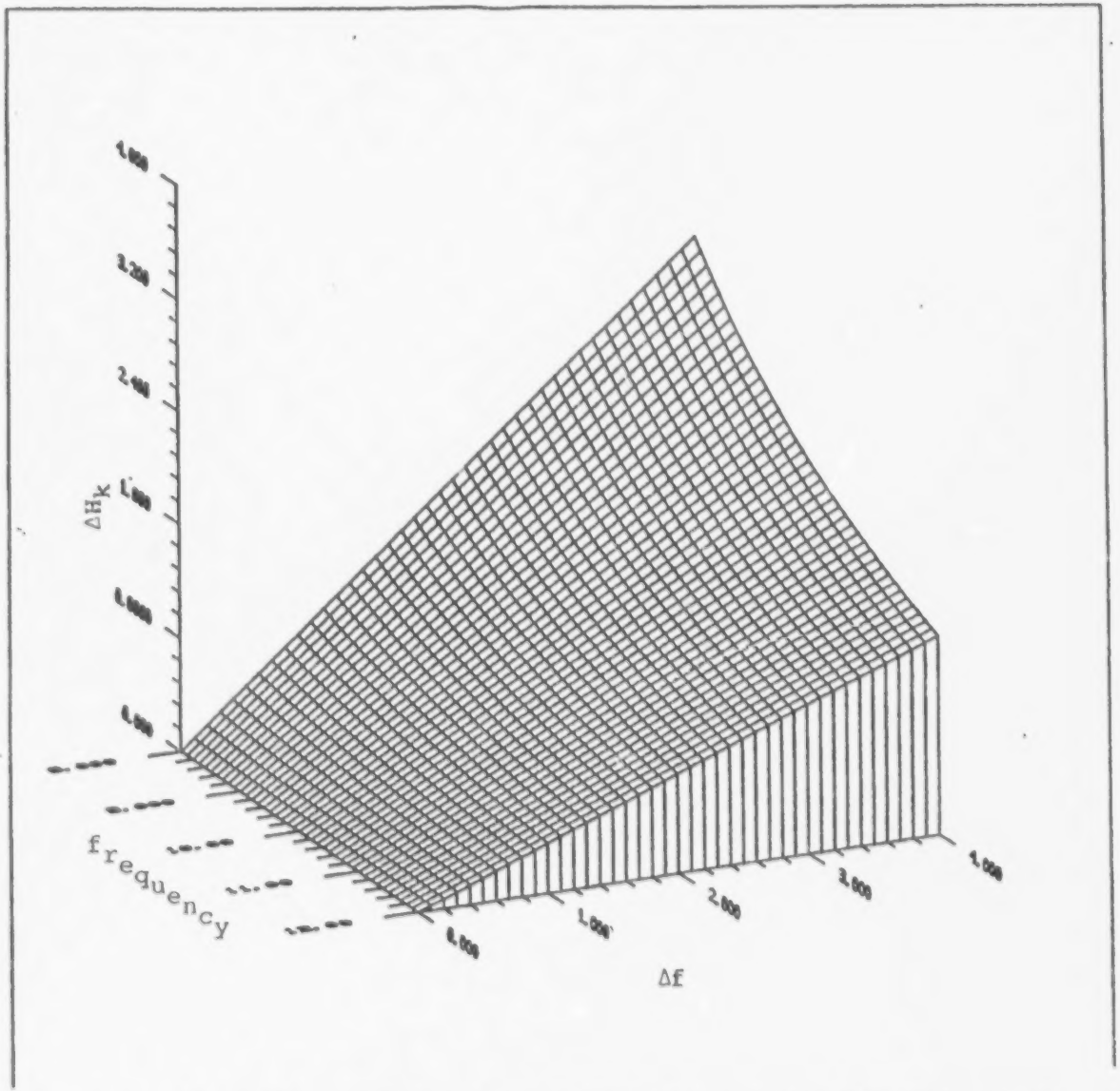

Figure 23: 3–dimensional surface plot representing alias tracks versus frequency and change in frequency.

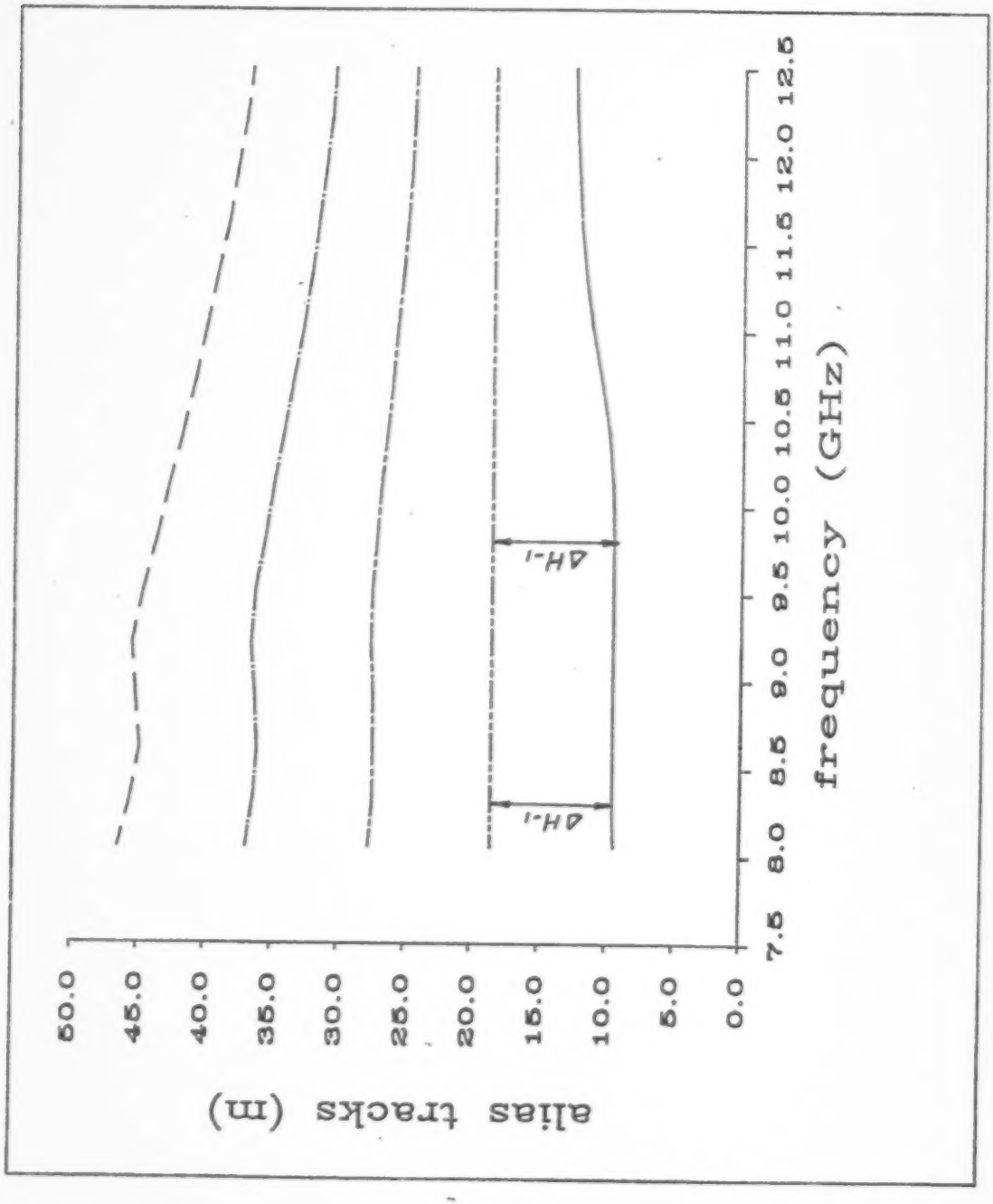

Figure 24: Alias tracks versus frequency for target height of 18.45 m

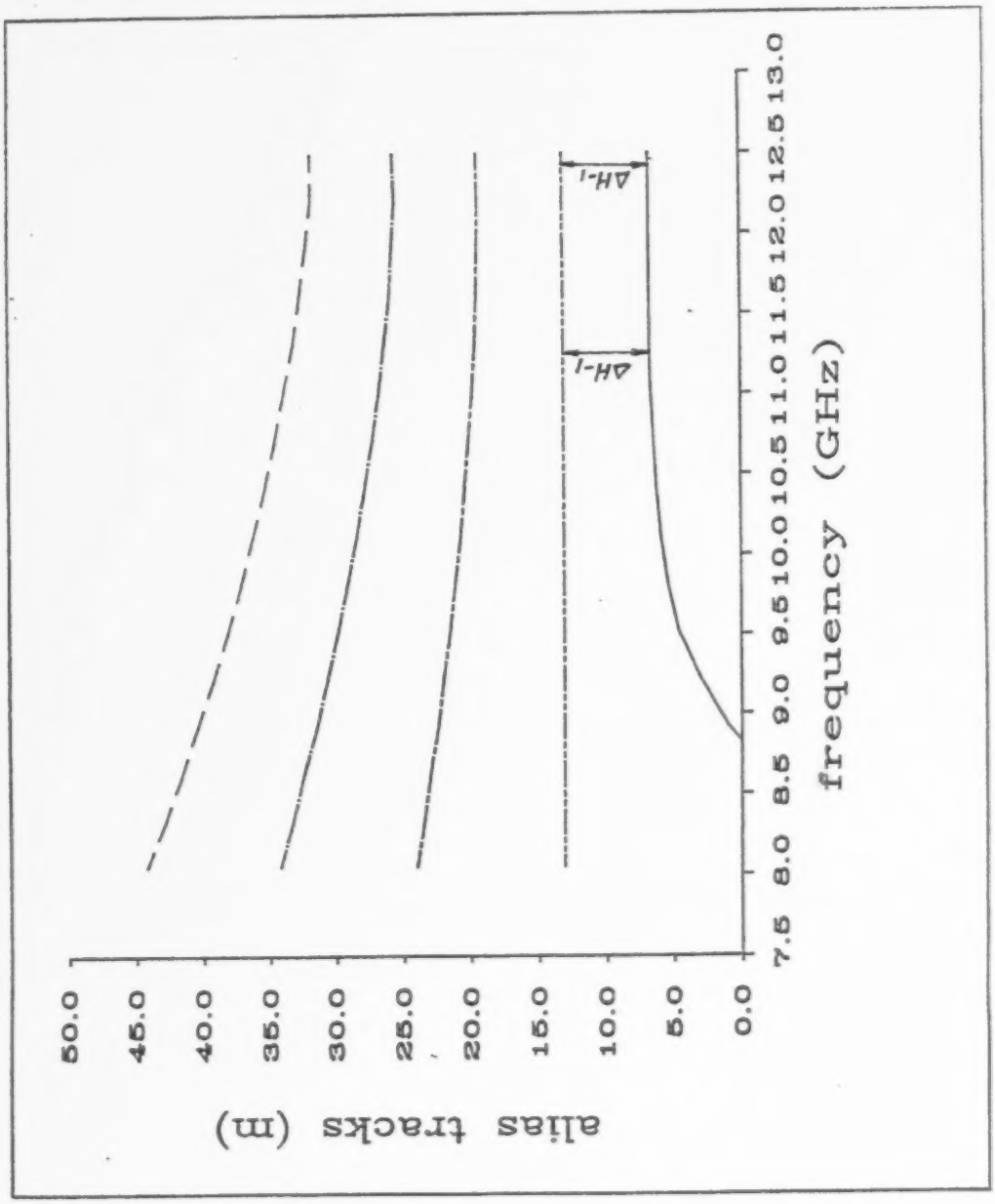

Figure 25: Alias tracks versus frequency.

P148367.PDF [Page: 71 of 80]

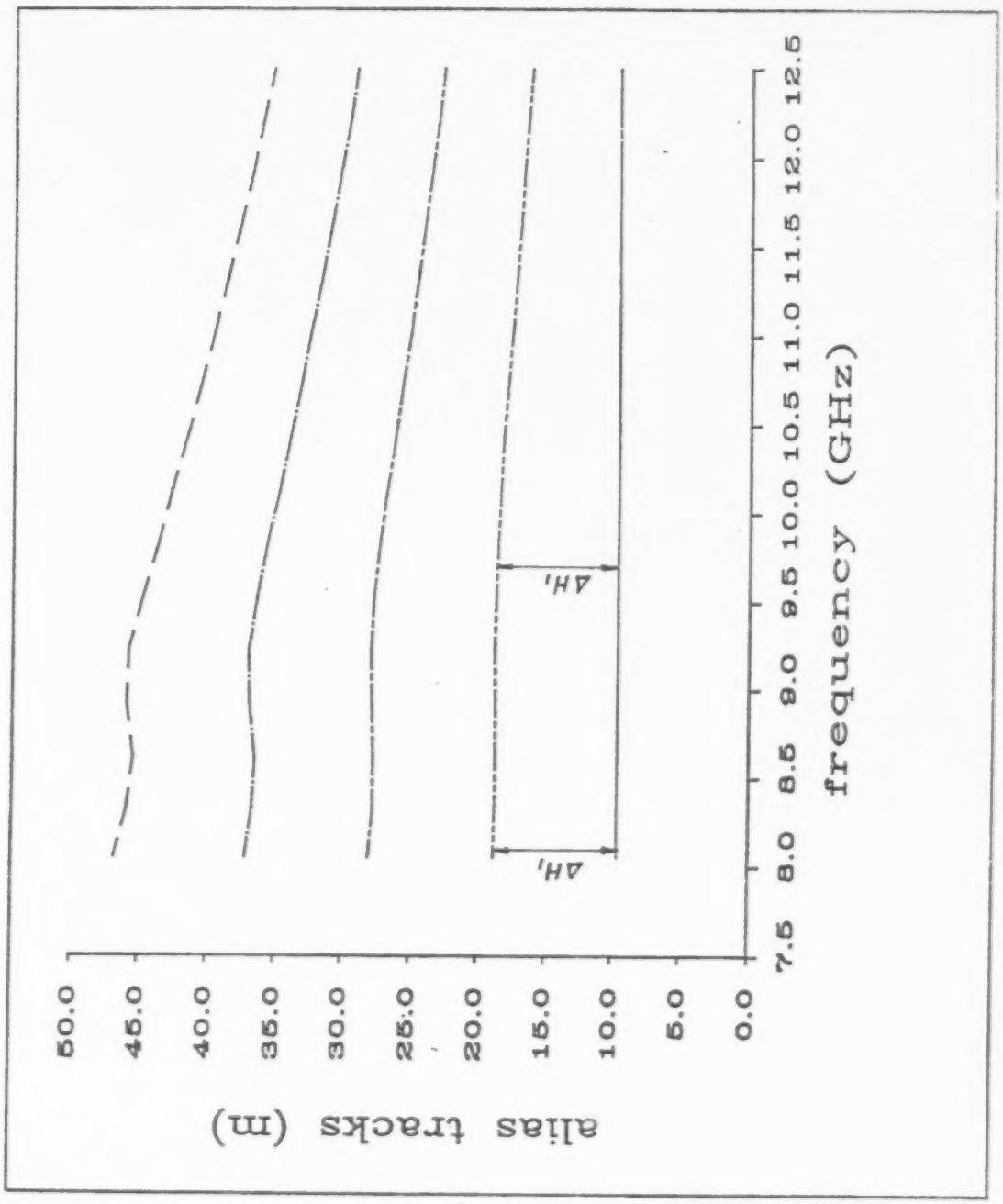

Figure 26: Alias tracks versus frequency.

P148367.PDF [Page: 72 of 80]

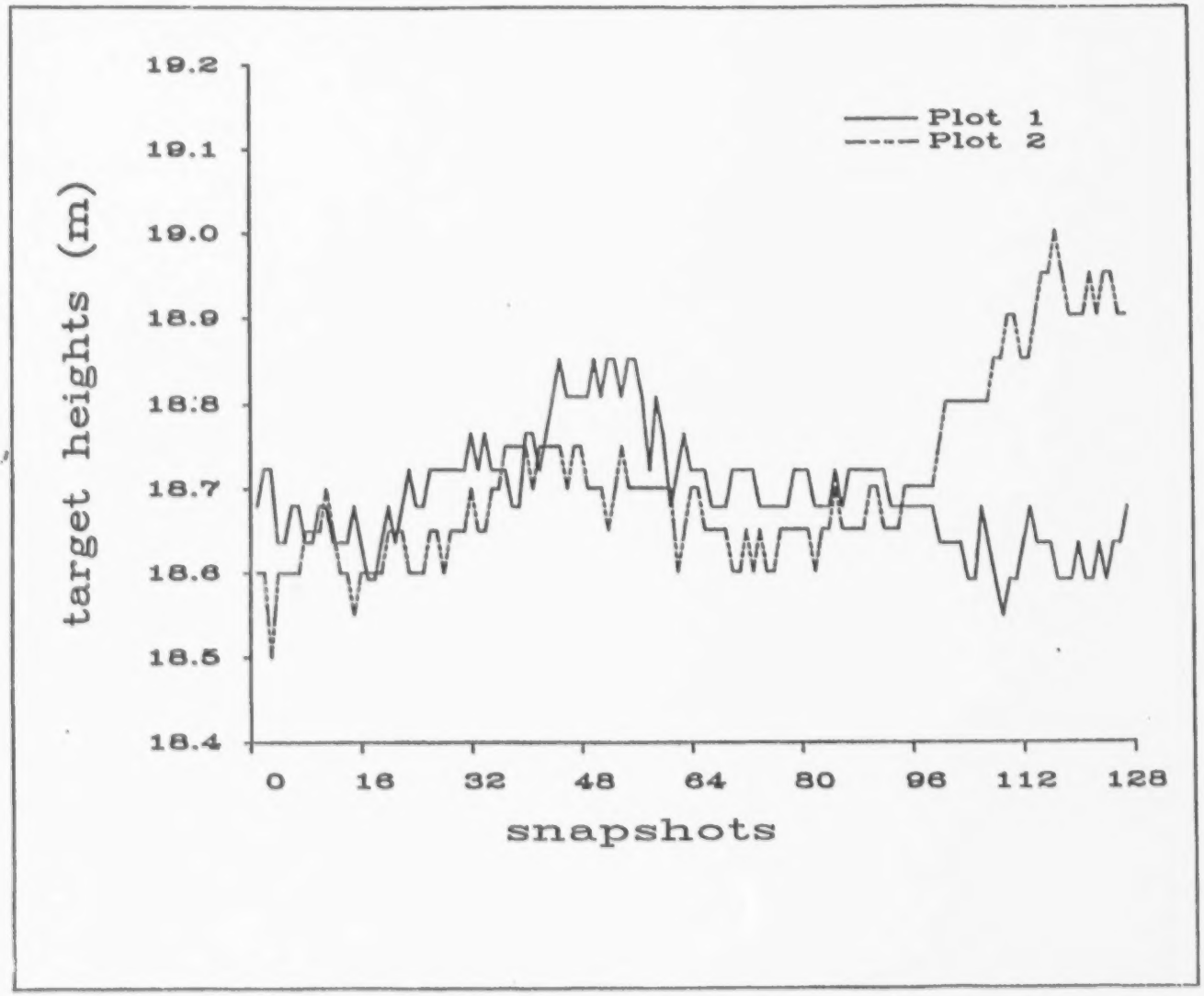

Figure 27: Target heights derived from CHA analysis: transmitter height=18.45 m, agile frequency = 11.92 GHz for Plot 1, agile frequency = 8.02 GHz for Plot 2.

P148367.PDF [Page: 73 of 80]

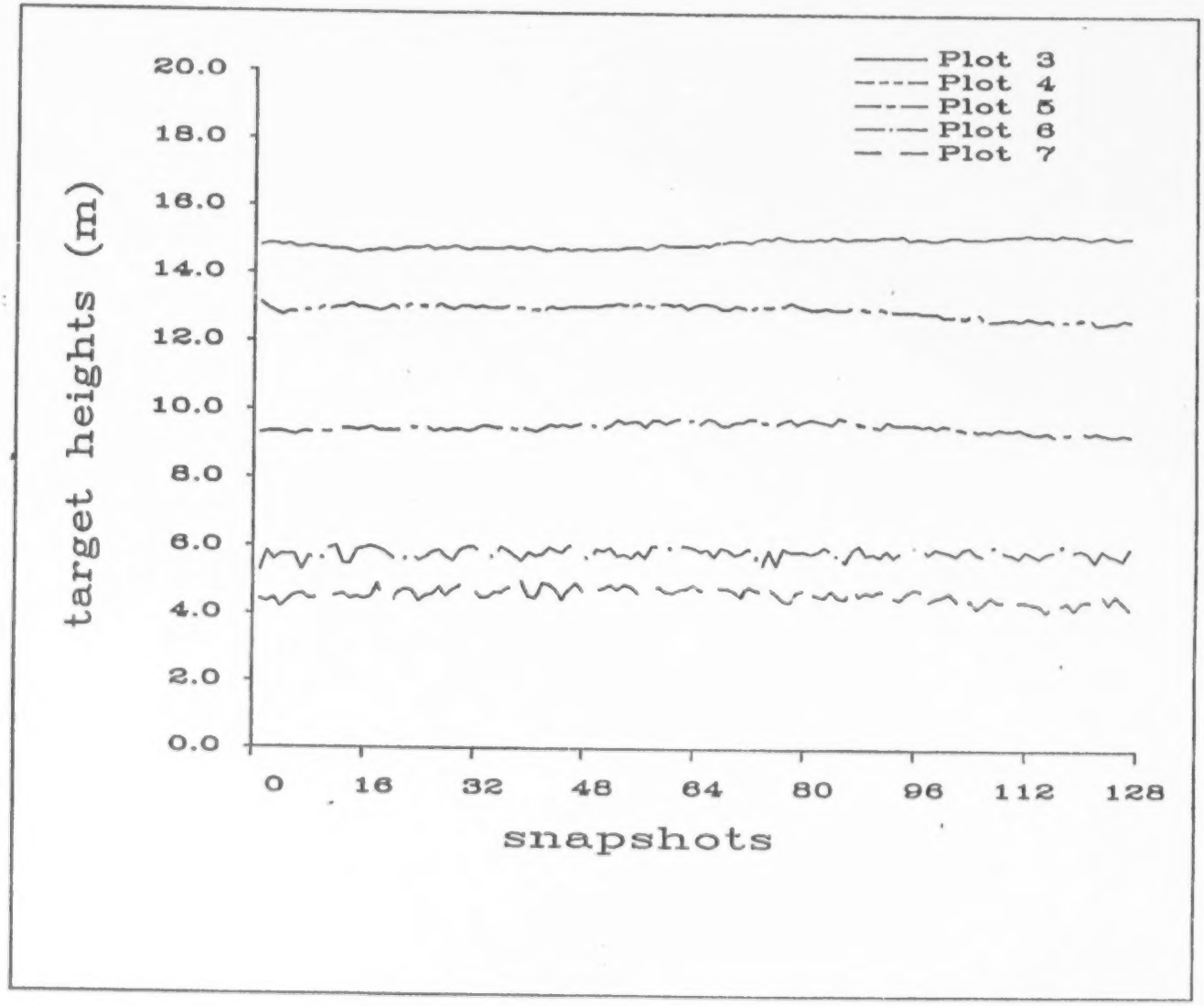

Figure 28: Target heights derived from CHA analysis: transmitter height=18.45 m for various agile frequencies.

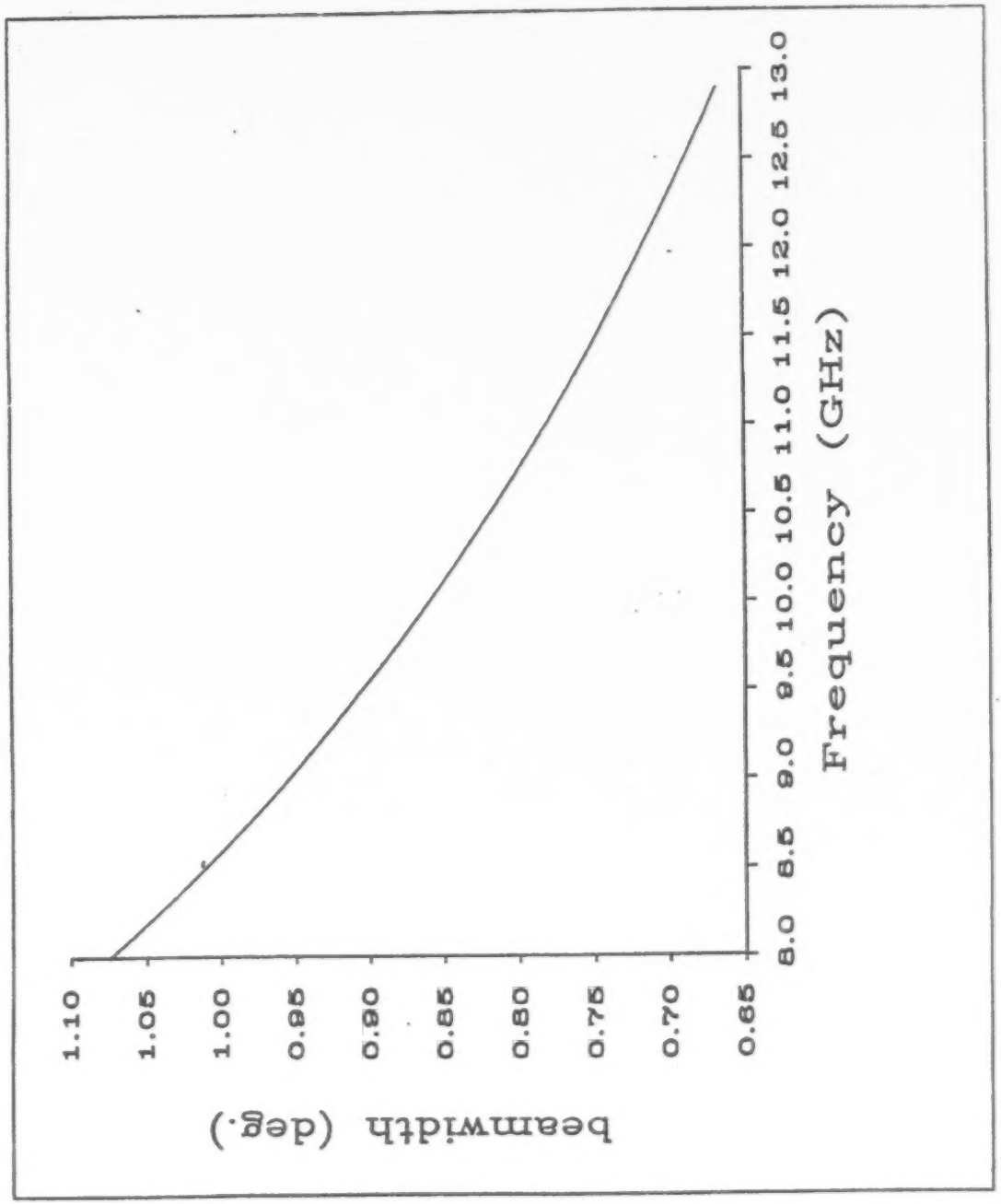

Figure 29: Beamwidth versus frequency for Figs. 23 and 24.

P148367.PDF [Page: 75 of 80]

Plot #	Tx Height (m)	Separation (% BW)	Estimated height* (m)	Relative discrepancy(%)	Variance
1	18.45	55.7	18.69	1.3	4.49×10^{-3}
2	18.45	48.2	18.71	1.4	1.11×10^{-2}
3	15.53	39.8	15.16	2.3	3.86×10^{-3}
4	13.06	32.2	12.96	1.5	1.99×10^{-2}
5	9.53	35.5	9.54	0.1	1.99×10^{-2}
6	6.50	16.0	5.85	10.0	2.62×10^{-2}
7	4.31	11.0	4.669	6.7	3.33×10^{-2}

* mean values

Table 5–1: Statistics of CHA results for Figs. 23 and 24.

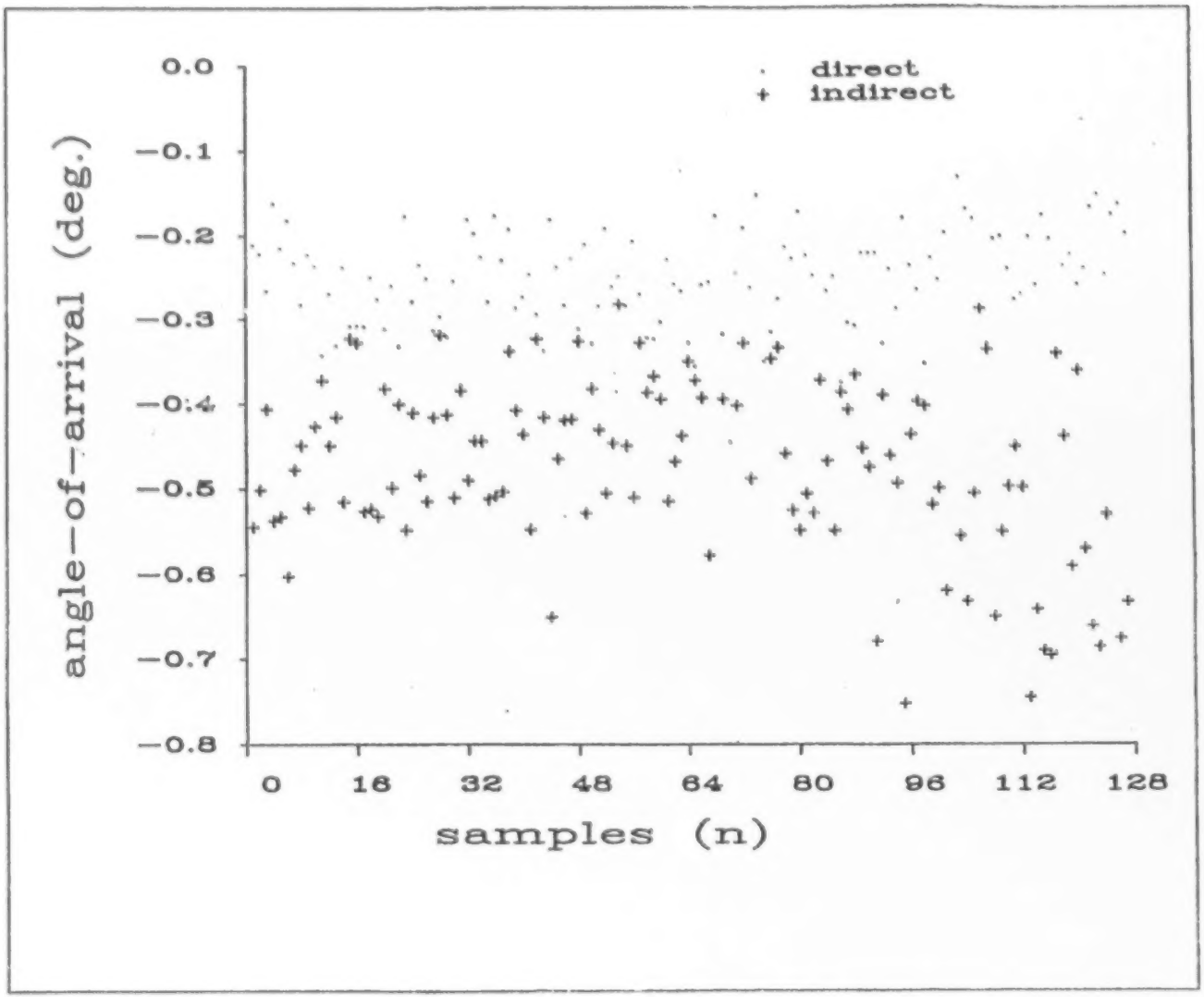

Figure 30: Angle–of–arrival estimates obtained from Principal Eigenvector Gram–Schmid method.

P148367 PDF [Page: 76 of 80]

UNCLASSIFIED
SECURITY CLASSIFICATION OF FORM
(Highest classification of Title, Abstract, Keywords)

DOCUMENT CONTROL DATA

(Security classification of title, body of abstract and indexing annotation must be entered when the overall document is classified)

1. ORIGINATOR (the name and address of the organization preparing the document. Organizations for whom the document was prepared, e.g. Establishment sponsoring a contractor's report, or tasking agency, are entered in section 8.)

McMaster University, 1280 Main Street West, Hamilton, Ont. L8S 4K1

2. SECURITY CLASSIFICATION (overall security classification of the document. Including special warning terms if applicable)

UNCLASSIFIED

3. TITLE (the complete document title as indicated on the title page. Its classification should be indicated by the appropriate abbreviation (S,C,R U) in parentheses after the title.)

Sea Swell Modelling, Collection and Analysis of Data (U)

4. AUTHORS (Last name, first name, middle initial. If military, show rank, e.g. Doe, Maj. John E.)

P. Bauman, J. Litva, L. Lai and T. Lo (Scientific Authority: Eloi Bossé)

5. DATE OF PUBLICATION (month and year of publication of document)

March 1989

6a. NO. OF PAGES (total containing information. Include Annexes, Appendices, etc.)

70

6b. NO. OF REFS (total cited in document)

10

7. DESCRIPTIVE NOTES (the category of the document, e.g. technical report, technical note or memorandum. If appropriate, enter the type of report, e.g. interim, progress, summary, annual or final. Give the inclusive dates when a specific reporting period is covered.)

Technical Report

8. SPONSORING ACTIVITY (the name of the department project office or laboratory sponsoring the research and development. Include the addre

Defence Research Establishment, Ottawa, 3701 Carling Ave, Ottawa, Ont. K1A 0Z4

9a. PROJECT OR GRANT NO. (if appropriate, the applicable research and development project or grant number under which the document was written. Please specify whether project or grant)

011LA

9b. CONTRACT NO. (if appropriate, the applicable number unde which the document was written)

20ST.W7714-6-5222

10a. ORIGINATOR'S DOCUMENT NUMBER (the official document number by which the document is identified by the originating activity. This number must be unique to this document.)

10b. OTHER DOCUMENT NOS. (Any other numbers which may assigned this document either by the originator or by the sponsor)

11. DOCUMENT AVAILABILITY (any limitations on further dissemination of the document, other than those imposed by security classification)

(X) Unlimited distribution
( ) Distribution limited to defence departments and defence contractors; further distribution only as approved
( ) Distribution limited to defence departments and Canadian defence contractors; further distribution only as approved
( ) Distribution limited to government departments and agencies; further distribution only as approved
( ) Distribution limited to defence departments; further distribution only as approved
( ) Other (please specify):

12. DOCUMENT ANNOUNCEMENT (any limitation to the bibliographic announcement of this document. This will normally correspond to the Document Availability (11). However, where further distribution (beyond the audience specified in 11) is possible, a wider announcement audience may be selected.)

13. ABSTRACT (a brief and factual summary of the document. It may also appear elsewhere in the body of the document itself. It is highly desirable that the abstract of classified documents be unclassified. Each paragraph of the abstract shall begin with an indication of the sec classification of the information in the paragraph (unless the document itself is unclassified) represented as (S), (C), (R), or (U). It is not necessary to include here abstracts in both official languages unless the text is bilingual).

In this report, the theoretical and practical issues involved in simulating multipath from sea swell surfac are extended and refined leading to a currently functional sea swell model. Consistent behavior is obse regarding null location and spacing, and the interference pattern is seen to be a function of sea state as as well as grid resolution. The report also features analysis of experimental data obtained from the Lak Huron trials of Fall 1987. This data, as well as that obtained at the Lake Ontario site during Fall 1988 trials, may be used in future validation of the described sea swell model.

14. KEYWORDS, DESCRIPTORS or IDENTIFIERS (technically meaningful terms or short phrases that characterize a document and could be he in cataloguing the document. They should be selected so that no security classification is required. Identifiers, such as equipment model designation, trade name, military project code name, geographic location may also be included. If possible keywords should be selected f published thesaurus. e.g. Thesaurus of Engineering and Scientific Terms (TEST) and that thesaurus-identified. If it is not possible to selec indexing terms which are Unclassified, the classification of each should be indicated as with the title.)

Multipath Modeling
Tracking Radars
Sea Swell
Scattering